

Widespread wildfires linked to early Albian Ocean Anoxic Event 1b

Xu, Xiaotao; Shao, Longyi; Eriksson, Kenneth; Zhou, Jiamin; Wang, Dongdong; Hou, Haihai; Hilton, Jason; Wang, Shuai; Lu, Jing; Jones, Timothy

DOI:
[10.1016/j.gloplacha.2022.103858](https://doi.org/10.1016/j.gloplacha.2022.103858)

License:
Creative Commons: Attribution-NonCommercial-NoDerivs (CC BY-NC-ND)

Document Version
Peer reviewed version

Citation for published version (Harvard):
Xu, X, Shao, L, Eriksson, K, Zhou, J, Wang, D, Hou, H, Hilton, J, Wang, S, Lu, J & Jones, T 2022, 'Widespread wildfires linked to early Albian Ocean Anoxic Event 1b: evidence from the Fuxin lacustrine basin, NE China', *Global and Planetary Change*, vol. 215, 103858. <https://doi.org/10.1016/j.gloplacha.2022.103858>

[Link to publication on Research at Birmingham portal](#)

General rights

Unless a licence is specified above, all rights (including copyright and moral rights) in this document are retained by the authors and/or the copyright holders. The express permission of the copyright holder must be obtained for any use of this material other than for purposes permitted by law.

- Users may freely distribute the URL that is used to identify this publication.
- Users may download and/or print one copy of the publication from the University of Birmingham research portal for the purpose of private study or non-commercial research.
- User may use extracts from the document in line with the concept of 'fair dealing' under the Copyright, Designs and Patents Act 1988 (?)
- Users may not further distribute the material nor use it for the purposes of commercial gain.

Where a licence is displayed above, please note the terms and conditions of the licence govern your use of this document.

When citing, please reference the published version.

Take down policy

While the University of Birmingham exercises care and attention in making items available there are rare occasions when an item has been uploaded in error or has been deemed to be commercially or otherwise sensitive.

If you believe that this is the case for this document, please contact UBIRA@lists.bham.ac.uk providing details and we will remove access to the work immediately and investigate.

Widespread wildfires linked to early Albian Ocean Anoxic Event

1b: Evidence from the Fuxin lacustrine basin, NE China

Xiaotao Xu^{a, b}, Longyi Shao^{a, *}, Kenneth A. Eriksson^c, Jiamin Zhou^a, Dongdong Wang^d,
Haihai Hou^e, Jason Hilton^f, Shuai Wang^e, Jing Lu^a, Timothy P. Jones^g

^a College of Geoscience and Surveying Engineering, China University of Mining and
Technology (Beijing), Beijing 100083, China

^b Shandong Key Laboratory of Depositional Mineralization & Sedimentary Mineral, Shandong
University of Science and Technology, Qingdao 266590, China

^c Department of Geosciences, Virginia Tech, Blacksburg, Virginia 24061, USA

^d College of Earth Science and Engineering, Shandong University of Science and Technology,
Qingdao 266590, China

^e College of Mining, Liaoning Technical University, Fuxin 123000, China

^f School of Geography, Earth and Environmental Sciences, University of Birmingham,
Edgbaston, Birmingham, B15 2TT, UK

^g School of Earth and Environmental Sciences, Cardiff University, Cardiff, CF10, 3YE, Wales,
UK

*** Correspondence author**

E-mail address: ShaoL@cumtb.edu.cn

Abstract

Wildfires are an important source of disturbances in the Earth's system and are of great
significance for understanding the interactions between environmental, atmospheric and
vegetation changes over deep time. The early Cretaceous was a "high-fire" interval with
frequent and widespread wildfires globally, but the timing and global significance of these
wildfire events during this time remain uncertain. We undertook a multi-proxy study
evaluating kerogen macerals, inertinite reflectance, and polycyclic aromatic hydrocarbons

(PAHs) from mudstones to characterize wildfire activity in the Albian coal-forming Fuxin lacustrine Basin, and correlate these with (i) environmental and floral changes on land, and (ii) well-dated marine events including the early Albian Oceanic Anoxic Event 1b (OAE 1b), to consider their environmental and climatic significance. The presence of high inertinite contents demonstrate that multiple, widespread wildfire events occurred during the early Albian, which are correlated stratigraphically to the Kilian, Paquier and Leenhardt sub-events of the early Albian OAE 1b. Inertinite reflectance values ranging from 0.6% to 3.8%Ro show that wildfires in the early Albian were dominated by ground fires, with a smaller proportion of surface fires and almost no crown fires. Atmospheric oxygen concentration (pO_2) levels, estimated from inertinite contents, attained ~25% during the early Albian, which exceeded the present atmospheric oxygen level of 21% and was able to support sustained combustion. Climatic conditions and frequent wildfire activity in the early Albian might have acted as an important control on vegetation distribution and diversification, which possibly further promoted the evolution of early angiosperms during the early Cretaceous. Wildfire activity resulted in the burning and destruction of both vegetation and soil structure, enhancing the post-fire erosion associated with intensified continental weathering under warmer and more humid conditions during the early Albian OAE 1b interval. These episodes of high wildfire activity correlate with high nutrients and organic matter levels in lakes and thereby contributed to eutrophication and anoxia in lacustrine and in contemporaneous oceanic systems.

Keywords

Cretaceous; early Albian; Fuxin Basin; wildfires; inertinite; Ocean Anoxic Event 1b

1. Introduction

Wildfires have played an important role in Earth system changes since the Silurian period when land plants first appeared on Earth and profoundly influenced global ecosystem patterns and processes (Glasspool et al., 2004; Glasspool et al., 2015; Lu et al., 2021). Charcoal, as the byproduct of wildfires, is recorded from the late Silurian (~420 Ma) to the present (Scott and Glasspool, 2006) and provides evidence for wildfire events in the rock fossil record (Scott and Glasspool, 2007; Scott, 2010; Shao et al., 2012; Wang et al., 2019a; Wang et al., 2021a).

Fusinite and semifusinite, the most frequent members of the inertinite maceral group, are believed to be the product of incomplete combustion from wildfires and were regarded as fossil charcoal in previous studies (e.g., Bustin and Guo, 1999; Scott, 2002). Some maceral formation mechanisms in inertinite, such as macrinite, may be related to fungal and/or bacterial degradation and/or arthropod ingestion and excretion (Hower et al., 2013). Although the origin of inertinite is still under frequent debate, more recent studies have concluded that inertinite is synonymous with charcoal and is almost exclusively considered as the byproduct of wildfires (e.g., Scott and Glasspool, 2007; Diessel, 2010; Glasspool and Scott, 2010; Glasspool et al., 2015). Inertinite is common throughout much of the Cretaceous Period (Diessel, 2010; Wang et al., 2021a), and recent evidence indicates widespread and frequent wildfires occurred during the Cretaceous (Bond and Scott, 2010; Brown et al., 2012; Sender et al., 2014; Moore et al., 2021; Wang et al., 2019b, 2021b). Thus, the Cretaceous has been considered as a “high-fire” world (Brown et al., 2012).

Polycyclic Aromatic Hydrocarbons (PAHs) in sediments are a powerful proxy for the identification of wildfire process throughout geologic history (e.g., Grice et al., 2007; Marynowski and Simoneit, 2009; Zakir Hossain et al., 2013; Zhou et al., 2021). Numerous studies have shown that unsubstituted PAHs, mostly consisting of 3–6 rings, can be used to indicate pyrogenic sources from combustion of organic matter (Page et al., 1999; Liu et al., 2005; Denis et al., 2012; Xu Y, et al., 2020a). High levels of PAHs are noted in various Cretaceous successions adding further support to the Cretaceous being a “high fire” interval (Finkelstein et al., 2005; Boudinot and Sepúlveda, 2020).

Wildfires respond strongly to atmospheric oxygen concentration (pO_2), and variations in the occurrence and abundance of inertinite in the Earth’s history have been used to estimate pO_2 levels (Jones and Chaloner, 1991; Wildman et al., 2004; Belcher et al., 2010; Glasspool and Scott, 2010; Shao et al., 2012; Glasspool et al., 2015; Hou et al., 2020; Wang et al., 2021a). Related studies have revealed that pO_2 above the present-day level of 21% would enable fuels to burn more frequently, while pO_2 levels below 18.5% would suppress fire frequency (Belcher et al., 2010). Wildfire is a significant evolutionary force that has shaped global biome distribution through geological time, and increased wildfire activity has been linked to the abundance of gymnosperms and the emergence of angiosperms (Bond and Scott,

2010; Brown et al., 2012). Conifer forests were abundant throughout the Cretaceous Period (e.g., Harland et al., 2007; Friis et al., 2010) from which wildfires have been hypothesized as opening up Cretaceous forests and promoting the expansion of early angiosperms (Bond and Scott, 2010; Belcher and Hudspeth, 2016). Additionally, direct and indirect evidence shows that angiosperms created novel wildfire regimes with positive feedbacks leading to more frequent wildfires, which would have facilitated their further diversification and spread (Bond and Scott, 2010; Belcher and Hudspeth, 2016; Belcher et al., 2021).

The early Albian Oceanic Anoxic Event 1b (OAE 1b) has been widely identified in multiple marine organic-rich sedimentary successions and carbon isotope excursions (Trabucho Alexandre et al., 2011; Coccioni et al., 2014) that represent major disturbances in the global carbon cycle (Jenkyns, 2010). The phenomenon of increased inertinite contents at the onset of Oceanic Anoxic Events (OAEs) has also been observed (Baker et al., 2017), which has provided evidence for enhanced wildfire activity in terrestrial settings during the OAEs onset. According to the model of Handoh and Lenton (2003), increased organic carbon burial across OAEs would have led to a gradual rise in pO_2 level and an increase in wildfire activity. Wildfires can result in the burning and destruction of land surface vegetation and soil structures (Brown et al. 2012), which increases the erosion potential and the flux of terrestrial organic matter and nutrients into the oceans, contributing to oceanic planktonic blooms and associated anoxic events (Brown et al. 2012; Glasspool et al., 2015; Yan et al., 2019; Xu et al., 2020a).

Numerous past studies have focused on sedimentary environments, palaeontology, tectonic evolution and coal accumulation in the Lower Cretaceous continental coal-bearing series of the Fuxin Basin (e.g., Chen et al., 1981; Guo, 1988; Liu et al., 1992; Wang et al., 1998; Zhu et al., 2007; Cai et al., 2011; Xu et al., 2020b), making these continental strata ideal for analyzing palaeoclimate and palaeoenvironmental changes during this time. Nevertheless, few studies have focused on wildfire activity in the Lower Cretaceous, and the possible relationships between wildfires, plant evolution, and anoxic events. In this paper, we conduct analyses of kerogen macerals, inertinite reflectance, PAHs of mudstones from the early Cretaceous Shaihai and Fuxin formations in the Fuxin Basin. Based on these data, we identify wildfire records and wildfire types, and attempt to estimate pO_2 levels from inertinite contents and to speculate on the role of wildfires not only on plant evolution, but also on the early

Albian OAE 1b. This is important for linking synchronous environmental changes on land and in the oceans to better understand their relationships with one another.

2. Geological setting

The continental Fuxin Basin is located in western Liaoning Province, northeastern China, on the northeastern part of the North China Plate (NCP) (Fig. 1a, b; Zhu et al., 2007). During the Jurassic–Cretaceous, the northeastern NCP was located in a back-arc setting and strongly influenced by subduction of the Palaeo-Pacific Plate (Fig. 1c; e.g., Zhu et al., 2017; Su et al., 2021). The Lower Cretaceous represents a peak period of rifting and magmatism in the northeastern NCP (Wu et al., 2014; Zhu et al., 2017). The Fuxin Basin is a fault-bounded basin that formed from rifting in the late Jurassic to early Cretaceous (Liu et al., 1992; Wang et al., 1998). The basin is bounded by the Lvshan Fault to the east and the Songling Fault to the west (Zhu et al., 2007), and extends from Shala city in the north to the Dalinghe Fault in the south (Fig. 2a). During the early Cretaceous the Fuxin Basin was at a palaeolatitude of ~40–45°N (Zhou et al., 2003; Li and Jiang, 2013).

The Lower Cretaceous sedimentary rocks in the Fuxin Basin comprise the Yixian, Jiufotang, Shahai, Fuxin, and Sunjiawan formations from oldest to youngest (Fig. 2b; Wan et al., 2013). In this study, the Shahai and Fuxin formations were selected to investigate continental wildfire records. The Shahai Formation mainly consists of mudstone, sandstone and conglomerate, with minor coal seams developed that were deposited in a continually expanding lacustrine basin (Zhu et al., 2007). From the bottom to the top, the Shahai Formation is subdivided into four members according to their lithological association (Li, 1988). The first and second members are mainly composed of conglomerates and coarse-grained sandstones that formed in an alluvial fan depositional system. The third member predominantly consists of sandstones and coal seams and formed in fan delta and lacustrine depositional systems. The fourth member is composed of thick-bedded black mudstones and fine-grained sandstones and is dominated by lacustrine depositional systems (Fig. 3; Guo, 1988; Zhu et al., 2007; Cai et al., 2011). The Fuxin Formation is predominantly composed of sandstones and mudstones with coal seams. It was deposited in fluvial and swamp sedimentary environments (Fig. 3; Xu et al., 2020b).

U-Pb zircon ages of the Yixian Formation from volcanic samples have been dated at 131–119 Ma (Xu et al., 2012; Zhang et al., 2016; Su et al., 2021; Fig. 2). Tuff samples from the Jiufotang Formation have given ages of 121–120 Ma (He et al., 2004; Su et al., 2021; Fig. 2). Zircon U-Pb dating of the tuffaceous claystone near the bottom of the fourth member of the Shahai Formation from the DY-1 borehole (1225.5m) gave an age of 112.6 ± 1.7 Ma (Fig. 3; Xu et al., 2022). This age constrains the fourth member of the Shahai Formation to the early part of the Albian Stage. Basalt samples at the top of the Fuxin Formation have yielded $^{40}\text{Ar}/^{39}\text{Ar}$ ages between 105.5 and 102.2 Ma (Zhu et al. 2004). These isotopic ages demonstrate that the Yixian, Jiufotang, Shahai and Fuxin formations are of Lower Cretaceous age. In China, the Lower Cretaceous is divided into the Jibei, Jehol and Liaoix regional stratigraphic stages (Wan et al., 2013). Of these, the Liaoix regional stage includes the Shahai, Fuxin and Sunjiawan formations in ascending stratigraphic order, and contains the Fuxin flora (Fig. 2b). The Fuxin flora is dominated by ferns, Ginkgoales and conifers, with abundant cycads and Equisetales and some angiosperms. It has been divided into three floral assemblages (Deng et al. 2012) in which the composition and diversity of angiosperms increase through the early Cretaceous (Tao et al., 2013). The Shahai Formation contains the *Acanthopteris-Ginkgo coriacea* assemblage, while the lower-middle part of the Fuxin Formation contains the *Ruffordia goepperti-Dryopterites* assemblage, and the upper part of the Fuxin Formation contains the *Ctenis lyrata-Chilinia* assemblage (Deng et al. 2012). The ages of all three floral assemblages are Lower Cretaceous (Chen et al., 1988; Deng and Chen, 2001), with the Shahai and Fuxin formations dated as late Aptian to Albian in age based on biostratigraphic and lithostratigraphic correlation (Deng et al., 2012; Xi et al., 2019).

Historically, it has been difficult to correlate well-dated marine strata with continental successions. The abundance of radiometric dates from Lower Cretaceous continental strata in the NCP (Fig. 2) provide a framework for its accurate correlation with marine strata. In Lower Cretaceous marine successions, OAE 1b is recognized from the late Aptian to the early Albian (~114.5–110.5 Ma) and is subdivided into four subevents; the uppermost Aptian Jacob, and the lower Albian Kilian, Paquier and Leenhardt sub-events (Coccioni et al., 2014; Li et al., 2016; Matsumoto et al., 2020). The sub-events can be recognized from perturbations of the global carbon cycle (Herrle et al., 2004; Navarro-Ramirez et al., 2015) that can be used for

chemostratigraphy and correlation with other areas. The early Albian aged Kilian, Paquier and Leenhardt sub-events are each characterized by distinct negative carbon isotope excursions (Herrle et al., 2004; Friedrich et al., 2005; Coccioni et al., 2014), while the late Aptian aged Jacob sub-event is defined by a weak negative carbon isotope excursion within the second late Aptian positive carbon isotope excursion (Coccioni et al., 2014; Herrle et al., 2015). In the Fuxin Basin, three distinct short-term negative excursions of organic carbon isotopes ($\delta^{13}\text{C}_{\text{org}}$) are recorded during the early Albian and are inferred to represent the Kilian, Paquier and Leenhardt sub-events of the early Albian OAE 1b (Xu et al., 2022).

3. Materials and methods

Mudstone samples analyzed in this study were collected from the DY-1 borehole (41° 52' 45" N - 121° 37' 8" E) in the central part of the Fuxin Basin (Fig. 2a). 54 mudstone samples were collected through the Shahai and Fuxin formations (Fig. 3). All samples were collected and stored in airtight, zip-lock plastic bags to avoid oxidation and contamination. Each mudstone sample was crushed to less than 1 mm diameter and then divided into two parts. One part was used for kerogen extraction (GB/T19144-2010) which was prepared as kerogen thin sections and polished epoxy-bound blocks. Identification of kerogen macerals was determined in thin sections under transmitted and fluorescent light using a Leica DM4500P LED microscope according to the China national standard (SY/T 5125-2014), with at least 300 valid points counted for each sample. Inertinite reflectance was measured on polished blocks using a Leica DM4500P LED reflected light microscope with a $\times 50$ oil immersion objective. For the inertinite reflectance measurements, at least 50 valid points were counted on each polished block. The remaining part of each mudstone sample was further crushed below 200 mesh (74 microns) for the analysis of PAHs. Aromatic hydrocarbon fractions were analyzed at the State Key Laboratory of Petroleum Resources and Prospecting at the China University of Petroleum in Beijing. Gas chromatography-mass spectrometry (GC-MS) analyses of the aromatic fractions were performed with an Agilent 7890GC/5975CMS following the test method for biomarkers in sediment and crude oil by GC-MS (GB/T 18606-2017). More details of the analysis method are described by Marynowski and Simoneit (2009) and Kang et al. (2020). For observation of homogenized cell walls, small mudstone fragments with charcoalfied plant

fossil fragments were mounted on a standard stub, coated with gold, and then observed under a SU8020 Scanning Electron Microscopy (SEM).

4. Results

4.1 Kerogen maceral compositions

Four types of macerals, including sapropelinite, vitrinite, exinite and inertinite, were observed in the mudstone samples from the Fuxin Basin (Fig. 4). Identification results of kerogen macerals (vol.%, mmf–mineral matter free) are given in Table 1 and Fig. 3. The sapropelinite content varies from 5.1 and 52.2 vol.% with an average of 27.5 vol.%, and under transmitted light microscopy is brownish yellow with flocculent edges (Fig. 4a and 4b). Vitrinite accounts for 43.7 vol.% in average, ranging from 16.6 to 75.3 vol.%. Under transmitted light microscopy, vitrinite is brownish red and does not fluoresce under fluorescence illumination (Fig. 4c and 4d). Exinite is not commonly observed, and ranges between 0 and 24.8 vol.% with an average value of 9.3 vol.%. Exinite mainly consists of spores and pollen grains that are yellowish brown in color, fluoresce under fluorescence illumination and exhibits various monomer forms, such as round, oval and triangular shapes (Fig. 4e-j). Inertinite contents range from 8.3 to 42.5 vol.% with an average of 19.5 vol.%, typically exhibiting shapes including cubic blocks and long strips with black color and silky luster (Fig. 5a-j). Under transmitted light microscopy, inertinite entirely consists of fusinite that are pure black in color, do not fluoresce under fluorescence illumination and occur as long strips or fragmental shapes with sharp and angular edges (Fig. 4k, 4l and 4m). Under reflected light microscopy of polished blocks, inertinites shows a prominent cellular structure or compressed and broken cell walls with relatively high reflectivity (Fig. 6). Under the SEM, inertinite exhibits homogenized (stratified in life) cell walls, while some cell walls are fractured, due to the compression associated with burial (Fig. 7).

To simplify the discussion and interpretation of the inertinite results, we subdivided the change trends into four units (Fig. 3) based on their overall composition. Unit A, which developed during the early part of the late Aptian, incorporates the first and second members of the Shahai Formation and is characterized by relatively low inertinite contents between 8.3 and 15.8 vol.%, with an average of 11.6 vol.%. Unit B, which developed during the latest Aptian

represents the third member of the Shahai Formation, has an increased inertinite content that varies from 8.4 to 20.3 vol.%, with an average of 12.9 vol.%. Unit C, which developed during the early Albian defines the fourth member of the Shahai Formation, is characterized by high inertinite contents that range from 14 to 42.5 vol.%. The average content of inertinite in the early Albian is 24.6 vol.% and is higher than that of the other three units. Unit D, which developed during the middle and late Albian defines the Fuxin Formation, is characterized by inertinite contents that range from 8.7 to 17.4 vol.% and display a downward trend.

4.2 Inertinite reflectance

The characteristics of inertinite reflectance from all mudstone samples are summarized in Table 1. Units A, B and C are characterized by relatively high values of inertinite reflectance ranging from 1.0–4.3%Ro, 0.8–3.4%Ro, and 0.6–3.8%Ro, respectively. Unit D is characterized by inertinite reflectance values that range from 0.8% to 2.6%Ro and display a decreasing trend upwards. Unit A contains a high proportion (89%) of inertinite with reflectance values between 1.8 and 3.5%Ro. In Unit B, most (69%) inertinite contents have reflectance values between 1.8 and 3.5%Ro, while 31% of inertinite contents have low reflectance values less than 1.8%Ro. Unit C comprises a proportion (35.5%) of inertinite reflectance between 1.8% and 3.5%Ro and a relatively high proportion (64.3%) of inertinite reflectance less than 1.8%Ro. In Unit D, most (81%) inertinite contents have reflectance values less than 1.8%Ro.

4.3 PAHs compounds

A total number of 18 PAHs were detected from ten selected mudstone samples (Fig. 8 and Table 2). The major PAHs compounds identified in all samples are I-Naphthalene, II-Fluorene, III-Biphenyl, IV-Dibenzothiophene, V-Dibenzofuran, VI-Phenanthrene, VII-Anthracene, VIII-Retene, IX-Fluoranthene, X-Benzo(a)fluorine, XI-Benzo(b)fluorine, XII-Pyrene, XIII-Benz(a)anthracene, XIV-Chrysene, XV-Benzofluoranthenes, XVI-Benzo(e)pyrene, XVII-Benzo(a)pyrene, and XVIII-Perylene with more or less intense methyl derivatives of the respective compounds. Quantitative analyses of PAHs show that total concentrations vary from 0.081 to 3.846 µg/g mudstone with an average of 1.836 µg/g mudstone (Table 2). Vertically through the succession, the PAHs compounds of Unit C are higher than those of the other three

units. In ten mudstone samples (Table 2), the high-molecular-weight of PAHs (5-ring) are identified, such as XVI-Benzo(e)pyrene (0.0004–0.1598 µg/g mudstone), XVII-Benzo(a)pyrene (0.0004–0.3 µg/g mudstone), and XVIII-Perylene (0–0.1878 µg/g mudstone).

5. Discussion

5.1 Evidence of wildfire

Evidence of wildfire is provided by analysis of inertinite (charcoal) and PAHs through the studied section.

5.1.1 Organic petrographic evidence of wildfire

Charcoal, the byproduct of wildfires, provides valuable information on the historical occurrence of wildfires (Scott and Glasspool, 2006; Glasspool and Scott, 2010). Inertinite is widely recognized as a synonym for charcoal and is widely accepted as direct evidence of wildfires in geological deep time (Scott and Glasspool, 2007). Although inertinite may originate from multiple paths (e.g., wildfires and degradation of organic matter), observations on modern charcoal deposits and experimental charring studies indicate that inertinite is formed almost exclusively as a product of wildfires (Jones et al., 1991; Jones, 1994; Scott and Glasspool, 2007).

Abundant charcoal particles from several microns to several centimeters were observed in hand specimens, in transmitted and reflected light microscopy and under the SEM (Figs. 4, 5, 6 and 7). These macroscopic and microscopic features are consistent with the characteristics of charcoal described by Scott (2010). In the study area, relative inertinite contents (8.3–42.5 vol.%) (Table 1) are very similar to relative inertinite values (mostly 10–45 vol.%) in coals from the Lower Cretaceous Erlian, Hailar, and Sanjiang basins in northeastern China (Wang et al., 2019b). Inertinite contents in Unit C are significantly higher than those in the other three units (Fig. 3). This observation provides evidence for an elevated wildfire activity during the early Albian interval. The vertical variation of inertinite abundances in this study (Fig. 3) indicates that wildfires were widespread and frequent in northeastern China during the Lower Cretaceous, which is consistent with the interpretation of Lower Cretaceous “high-fire” conditions especially during the early Albian (Bond and Scott 2010; Diessel, 2010; Brown et

al. 2012).

5.1.2 PAHs evidence of wildfire

PAHs are a class of compounds consisting of two or more benzene rings fused in a linear, angular, or clustered arrangement (Chefetz et al., 2000). PAHs originate from two main sources in sedimentary strata, including incomplete combustion of fossil fuels such as coal and petroleum, and other organic matter such as wood (Thompson et al., 2017), as well as degradation of organic matter by microorganisms during diagenesis (Zakir Hossain et al., 2013; Meng et al., 2019). PAHs from pyrogenic sources (combustion of organic matter) mainly consist of 3–6 ring PAHs, which are distinguished by high abundances of unsubstituted compounds (Page et al., 1999; Liu et al., 2005; Denis et al., 2012; Xu et al., 2020c). Unsubstituted PAHs have been extensively regarded as wildfire indicators in sedimentary rocks due to their pyrolytic origin (Liu et al., 2005; Grice et al., 2007; Marynowski and Simoneit, 2009; Zakir Hossain et al., 2013). However, the abundance of PAHs is likely to be affected by the thermal history of a basin, which should be seriously considered before interpreting the source of PAHs (Murchison and Raymond, 1989; Jiang et al., 1998; Zhang et al., 2020). Because of the influence of diabase intrusion on the sedimentary strata at the bottom of the Shahai Formation (Zhang et al., 2003; Zhu et al., 2007), the relatively high abundance of PAHs in units A and B might be considered to be the result of rapid heating of organic material by magmatic intrusions (Murchison and Raymond, 1989). In the study area, high-molecular-weight PAHs (3–5 ring) were identified, whereas the PAHs with 6-rings were not found. The occurrence of pyrogenic PAHs indicates that a wide range of wildfires occurred in the Fuxin Basin during the Lower Cretaceous, and the abundance of 3–5 ring PAHs indicates that wildfire activity in Unit C was more intense and frequent than for the other three units. Fluoranthene, pyrene, benz[a]anthracene, benzo[a]fluoranthene, benzo[e]pyrene, benzo[a]pyrene, indeno[1,2,3-cd]pyrene, benzo[ghi]perylene and coronene are commonly considered to be primarily of combustion origin (Zakir Hossain et al., 2013). The higher the number of aromatic rings, the stronger the antioxidant ability of PAHs (Xu et al., 2020c). Studies show that benzo[e]pyrene is highly resistant to oxidation processes (Marynowski et al., 2011) and is the most stable PAH among the 5-ring PAHs (Jiang et al., 1998; Sullivan et al.,

1989). The occurrence of PAHs with 5-rings in this study (Fig. 8) also indicates that a wide range of wildfires occurred in the Lower Cretaceous Fuxin Basin. PAH compounds show the different aromatic rings at different combustion temperatures (Zakir Hossain et al., 2013). The high abundances of high-molecular-weight PAHs represent a relatively high combustion temperature, which can provide information on wildfire intensity (Finkelstein et al., 2005; Denis et al., 2012; Zakir Hossain et al., 2013). In the study area, the relatively high abundance of PAHs with 5-rings (benzo[e]pyrene, benzo[a]pyrene and perylene) in Unit C during the early Albian mostly shows high wildfire intensity.

5.2 Wildfire types inferred from inertinite reflectance

Inertinites from wildfire activity show a range of reflectance values which are directly related to fire type and temperature (Scott and Jones, 1994; Jasper et al., 2016). Experimental data have demonstrated that high reflectance of inertinite may be the result of increasing temperature during wildfire activity (Jones et al., 1991; Scott and Glasspool, 2007). Although there is no absolute linear relationship between inertinite reflectance and burning temperature, a correlation has been expressed by a linear regression equation derived by Jones (1997): $T = 184.10 + 117.76 \times \%Ro$ ($r^2 = 0.91$). Where T is the burning temperature and %Ro is the measured inertinite reflectance.

Based on experimental data, the ranges of inertinite reflectance for units A, B, C and D are 1.0–4.3%Ro, 0.8–3.4%Ro, 0.6–3.8%Ro and 0.8–2.6%Ro, respectively. According to the above equation, the corresponding temperature ranges of inertinite formation are 303.4–696.2 °C, 275–589.7 °C, 255–626.8 °C and 278.7–485.7 °C, respectively. Wildfires can be grouped into three types by different burning temperatures, namely, ground fire, surface fire and crown fire (Scott and Jones, 1994; Petersen and Lindström, 2012; Wang et al., 2019b). Ground fires that burn organic material below the litter, generally produce maximum temperatures around 400 °C, while surface fires that burn litter and herbaceous and shrubby plants, can reach temperatures around 600 °C. Crown fires typically burn canopies of trees and larger shrubs, which can produce intense heat with temperatures of 800 °C or higher (Scott and Jones, 1994; Petersen and Lindström, 2012; Wang et al., 2019b). In the study area, mudstone samples in units A and B have seemingly circumvented the normal thermal history, with the increase of

inertinite reflectance being caused by rapid heating in an environment of magmatic intrusive activity (Murchison and Raymond, 1989). Therefore, units A and B were abandoned for analysis of inertinite reflectance, burning temperature and wildfire type. Although the range of the inertinite reflectance values in Unit C is wide, inertinite with low reflectance values between 0.6 and 1.8%Ro accounts for 64.3% of the inertinite content of Unit C. These inertinites have low burning temperatures between 255 and 400 °C, indicating that they are predominantly derived from ground fires (Petersen and Lindström, 2012; Fig. 10). In addition, inertinite with reflectance values between 1.8 and 3.5%Ro accounts for 35.5% of the total inertinite population in Unit C. Their formation temperatures are between 400 and 600 °C, inferring relatively high temperature surface fires (Petersen and Lindström, 2012; Fig. 10). According to Jones (1996) and Scott (2010), the cell walls of inertinite become homogenized above a temperature of 300–325 °C. In Unit C, the inertinite observed under SEM shows homogenized cell walls (Fig. 7), indicating that the burning temperature of wildfire was higher than 300–325 °C. In Unit D, the proportion of inertinite with reflectance values less than 1.8%Ro increases to 81%, while inertinite with reflectance values between 1.8 and 3.5%Ro accounts for 19% of the inertinite population of Unit D. These results indicate a decrease in burning temperatures through time in Unit D.

5.3 Atmospheric oxygen levels estimated from inertinite contents

Atmospheric oxygen concentration (pO_2) varied dramatically during the Mesozoic (Belcher and McElwain, 2008; Belcher et al., 2010; Mills et al., 2016). Based on models, elevated pO_2 levels have been proposed globally during the Albian (Bergman, 2004; Glasspool and Scott, 2010; Wang et al., 2019b) with a maximum value up to 29% (Glasspool and Scott, 2010), significantly higher than present-day 21% concentration (Belcher and McElwain, 2008; Belcher et al., 2010). Berner (2009) predicted pO_2 levels below present-day values until the Albian, thereafter, rising above 21%. Oxygen plays an important role in the occurrence of wildfires and the formation of inertinite (Scott, 2010; Shao et al., 2012; Glasspool et al., 2015; Yan et al., 2019). Experimental data reveal that fire activity would be entirely switched off below pO_2 levels of 16%, greatly suppressed below pO_2 levels of 18.5%, and rapidly enhanced between pO_2 levels of 19–22% (Belcher et al., 2010). If pO_2 significantly exceeded 25%, fire

frequencies would have been widespread and even globally in aerial extent (Wildman et al., 2004; Belcher et al., 2010). Previous studies considered that inertinite contents in the sedimentary record could be used to infer atmospheric pO_2 levels (e.g., Scott and Glasspool, 2007; Glasspool and Scott, 2010).

Glasspool and Scott (2010) and Glasspool et al. (2015) compiled a large database on inertinite contents of coals from different geological periods, and then proposed an inertinite to pO_2 calibration curve. Although this model is based on inertinites found in coals, the relative proportion of the inertinite in the kerogens contained in the mudstones may also give an approximation on the atmospheric oxygen level (Liu et al., 2020). In this study, the relative inertinite contents with an average of 24.6 vol.% from all mudstone samples in Unit C would indicate a pO_2 level of ~25% during the early Albian based on the model of Glasspool et al. (2015) (Fig. 11). The relative content of inertinites in contemporaneous coals of the Fuxin Basin ranged from 12% to 19% (Yang, 1996), and these inertinite contents would give a pO_2 level between approximately 23% to 24%. In addition, the pO_2 level estimated from the inertinite contents in the Albian coals of other regions in NE China is around 25.3% (Wang et al., 2019b). The results from coals and mudstones are very similar, and are in accordance with the models of Bergman et al. (2004), Arvidson et al. (2006) and Glasspool and Scott (2010) that estimated pO_2 levels in the early Albian atmosphere were around 25%. As a result, pO_2 level may be calculated from relative inertinite contents in mudstone, nevertheless, it needs to be used with caution. From this it can be interpreted that pO_2 levels during the early Albian were much higher than the minimum needed for sustained combustion, and even reached a situation where fires become common. The high pO_2 levels would have led to greatly increased plant flammability, which is consistent with a global record of widespread wildfires during the Lower Cretaceous (Belcher et al., 2010; Diessel, 2010; Wang et al., 2021a; Wang et al., 2019b, 2020b).

5.4 Contemporaneous wildfires and the evolution of early angiosperms

A growing body of fossil evidence documents angiosperms first evolved in the Lower Cretaceous and subsequently underwent a rapid radiation to gain ecological dominance by the Upper Cretaceous (e.g., Bond and Scott, 2010; Friis et al., 2010; Brown et al., 2012; Coiro et

al. 2019). The oldest recognized angiosperms from the megafossil record come from the Barremian aged Yixian Formation (Friis et al., 2010) from the North China Plate. However, while the megafossil record of Cretaceous angiosperms is often scant, records of their distinctive pollen demonstrate that the group first appeared in the Barremian at low paleolatitudes and diversified and spread into higher northern and southern paleolatitudes (Couper, 1958; Coiro et al., 2019). The earliest angiosperms appeared in the middle paleolatitudes during the Albian noted by the presence of pollen genera including *Cupuliferoideaepollenites*, *Fraxinoipollenites*, *Phimopollenites*, *Rousea* and *Tricolpites* (Korasidis et al., 2016), and reached high-latitude Arctic area during the Cenomanian including the pollen genera *Tricolpites* sp. and *Retitricolpites* sp. (Brenner, 1976; Galloway et al., 2012; Coiro et al. 2019).

In the North China Plate, Lower Cretaceous continental strata are widely-developed and contain abundant palynomorphs and excellently preserved angiosperm macrofossils which have been used for biostratigraphy and to explore early angiosperm evolution. Lower Cretaceous angiosperm pollen from the North China Plate has been subdivided into five distinct stages from the Barremian, Aptian, early and middle Albian, late Albian, and latest Albian–Cenomanian (Song, 1986). In the Barremian, the monosulcate angiosperm pollen *Clavatipollenites* began to appear in low numbers. During the Aptian, tricolpate angiosperm pollen appeared alongside *Clavatipollenites* but was relatively monotonous morphologically, with angiosperm pollen comprising approximately 5% of Aptian palynofloral assemblage (Song, 1986). In the early and middle Albian, tricolpate pollen types diversified markedly and included more complex forms, and the proportion of angiosperm pollen rose to approximately 10%. In the late Albian, tricolporate angiosperm pollen first appeared, with the proportion of the angiosperm pollen in palynofloras remaining at approximately 10%. The latest Albian–Cenomanian palynofloras are marked by the first appearance of oblate tricolporate and triplicate angiosperm pollens and the proportion of angiosperm pollen in palynofloras at this time exceeding 10% (Song, 1986). These five floral stages clearly show the diversification and rise in abundance of angiosperm pollen through the North China Plate during the Lower Cretaceous.

Looking more locally at the study area in western Liaoning Province, the Lower

Cretaceous has previously been divided into the Jibei, Jehol and Liaoxi regional stratigraphic stages (Wan et al., 2013; Fig. 2). Of these the Barremian–lower Aptian aged Jehol stage corresponds to the Yixian and Jiufotang formations and includes the stratigraphically oldest angiosperm megafossils (Friis et al., 2010) including *Archaeofructus sinensis* and *Sinocarpus decussatus* (Sun et al., 1998, 2002; Leng and Friis, 2003; Zhou et al., 2003; Hilton and Bateman, 2006). The upper Aptian-Albian aged Liaoxi regional stage corresponds to the Shapai, Fuxin and Sunjiawan formations in ascending order (Fig. 2). The Shapai and Fuxin formations contain the Fuxin flora that is dominated by ferns, Ginkgoales and conifers with abundant cycads and Equisetales and occasional angiosperms (Deng et al., 2012; Wan et al., 2013). However, despite the megaf flora of the Shapai and Fuxin formations being similar, the *Cicatricosisporites-Pinuspollenites-Classopollis* palynological assemblage in the Shapai Formation contains typical tricolpate angiosperm pollen including *Tricolpites* and *Tricolpopollenites* (Tao et al., 2013), while angiosperm pollen is abundant in the *Cicatricosisporites-Laevigatosporites-Piceapollenites* palynological assemblage in the lower part of the Fuxin Formation (Tao et al., 2013). Angiosperms with complex reticulate leaf venation including *Asiatifolium elegans*, *Chengzihella obovata*, *Jixia pinnatipartita*, *Shenkuoia claoneura* and *Rogersia lanceolata* (Sun et al., 1992) occur in the *Ruffordia goepperti-Dryopterites* assemblage from the lower-middle part of the Fuxin Formation (Deng et al. 2012). The upper part of the Fuxin Formation contains the *Ctenis lyrata-Chilinia* assemblage (Chen et al. 1988) in which angiosperms are relatively abundant and include *Populus* sp., *Vitiphyllum* sp. and *Trochodendroides* sp. (Deng et al. 2012). Finally, in the Sunjiawan Formation angiosperm pollen became a very common component *Appendicisporites-Laevigatosporites* assemblage (Tao et al., 2013). To summarize, the abundance and diversity of angiosperms show a distinct increase from the Yixian Formation to the Sunjiawan Formation during the early Cretaceous in the western Liaoning region.

Wildfires have existed as a significant evolutionary force that may have affected the nature of the vegetation itself (Bond and Keeley, 2005; Brown et al., 2012). Many plants have acquired adaptive traits that enable them to cope with fire and reproduce in fire-prone ecosystems (Bond and Scott, 2010; Brown et al., 2012; Belcher et al., 2021). Furthermore, previous studies have suggested that the spread and diversification of angiosperms in the

Cretaceous was facilitated by fire regimes (e.g., Bond and Scott, 2010; Friis et al., 2010; Brown et al., 2012). It is especially noteworthy that the earliest known fossil flowers are preserved as charcoalified mesofossils (e.g., Friis et al., 2010), further emphasizing the relationship of angiosperms with fire. The earliest angiosperms were weedy plants characterized by small herbaceous or shrubby habits with little wood that formed the understory and ground cover (Friis et al., 2010; Royer et al., 2010; Brown et al., 2012). Brown et al. (2012) proposed that herbaceous plants may allow surface fires to burn rapidly. In the study area, 35.5% of inertinite content of the early Albian have experienced relatively high burning temperature between 400 and 600 °C, indicating that they are mainly derived from surface fires. This type of wildfire may have had little effect on soils such that plant roots and seed banks may not have been killed, allowing for rapid regrowth of vegetation and especially herbaceous and shrubby plants following rainfall (Brown et al., 2012). Highly productive weedy angiosperms favour rapid fuel accumulation, which may promote shorter fire cycles under suitable physical preconditions (Bond and Scott, 2010). Frequent Cretaceous wildfires could open up adjacent closed environments and create open sunlit habitats favorable to the expansion of early angiosperms (e.g., Berendse and Scheffer, 2009; Bond and Scott, 2010; Belcher et al., 2021).

In the Lower Cretaceous of northeast China, the Fuxin flora from the Shahai and Fuxin formations provided an appropriate source of fuel for wildfires. The spores and pollen grains (Fig. 4e-j) and plant fossil fragments (Fig. 5k and 5l) observed in the early Albian Fuxin Basin also provide evidence for the existence of ferns, conifers and cycads characteristic of the Fuxin Flora. Angiosperms played an increasingly important role in Lower Cretaceous floras in NE China from the Barremian onwards increasing in abundance and diversity through time. The widespread wildfires in the Fuxin Basin during the early Albian coincide with the suggestion that wildfires may have played an important role in promoting the spread and diversification of early angiosperms in this region. In particular, we speculate that frequent surface fires could be conducive to the rapid recovery of the early low-stature angiosperms after burns during the early Albian.

Huang et al. (2007) proposed that elevated atmospheric CO₂ levels increases photosynthetic rates and rising *p*CO₂ has a positive effect on plant growth due to increasing

availability of carbon. Moreover, enhanced leaf vein densities in the evolution of early angiosperms also potentially increased maximum photosynthetic rates (Brodribb and Field, 2010). Elevated $p\text{CO}_2$ levels in the early Albian (Haworth et al., 2005; Hong and Lee, 2012; Sun et al. 2016; Barral et al., 2017; Xu et al., 2022) and high leaf vein densities during the Lower Cretaceous (Field et al., 2011) would have led to an increase in primary productivity, and consequently, greater fuel loads (He et al., 2018). Rapid accumulation of vegetation with high productivity and rapid recovery in the Lower Cretaceous would have provided an ample fuel source for the frequent occurrence of wildfires under high $p\text{O}_2$ levels, which further supports suggestions of a link between wildfires and the spread of early angiosperms.

5.5 Continental wildfires linked to the early Albian OAE 1b

OAE 1b is characterized by several short-term perturbations of the global carbon cycle and multiple black mudstone horizons with relatively enhanced organic carbon contents (Trabucho Alexandre et al., 2011). Stratigraphically, OAE 1b spans the late Aptian to early Albian (~110.5–114.5 Ma) and each perturbation corresponds to one of the four sub-events comprising the uppermost Aptian Jacob sub-event, and the lower Albian Kilian, Paquier and Leenhardt sub-events (Coccioni et al., 2014; Li et al., 2016; Matsumoto et al. 2020).

5.5.1 Recognition of the Jacob sub-event

The Jacob sub-event is the first organic-rich expression during OAE 1b (Coccioni et al., 2014; Matsumoto et al. 2020). In western Tethys, the Jacob sub-event is ~75 cm thick with a TOC content up to 2.5–8% (Herrle 2002; Heimhofer et al. 2006; Coccioni et al., 2014; Sabatino et al., 2015; Matsumoto et al. 2020). The Jacob sub-event is characterized by a weak negative carbon isotope shift within the second late Aptian positive carbon isotope excursion (Coccioni et al., 2014; Herrle et al., 2015). Matsumoto et al. (2020) conducted a comparative analysis of the negative $\delta^{13}\text{C}_{\text{carb}}$ excursion of the Jacob sub-event in western Tethys and the Pacific Ocean, indicating that it is marked by a weak negative $\delta^{13}\text{C}_{\text{carb}}$ shift of ~0.7‰ in western Tethys (Coccioni et al., 2014; Fig. 9).

In the study area, the Aptian/Albian boundary was placed at the boundary between Unit B and Unit C corresponding with an age greater than 112.6 ± 1.7 Ma according to zircon U-Pb

dating analyses (Fig. 9; Xu et al., 2022), constraining Unit B to the latest Aptian approximately. In the latest Aptian Fuxin Basin, a weak negative $\delta^{13}\text{C}_{\text{org}}$ excursion of -22.7‰ occurred in an interval of a positive $\delta^{13}\text{C}_{\text{org}}$ excursion near the Aptian/Albian boundary. The peak value of the negative $\delta^{13}\text{C}_{\text{org}}$ shift corresponds to a relatively high TOC value up to 1.1%. From this we interpret that the slight negative $\delta^{13}\text{C}_{\text{org}}$ excursion below the Aptian/Albian boundary may represent the Jacob sub-event (Fig. 9).

5.5.2 Recognition of the Kilian sub-event

The Kilian sub-event is the organic-rich expression of the second sub-event of OAE 1b (Coccioni et al., 2014). Most studied successions in western Tethys and eastern North Atlantic show that the thickness of the Kilian sub-event varies between ~38 cm and 80 cm with TOC contents ranging of ~1–5% (e.g., Herrle, 2002; Herrle et al., 2004; Friedrich et al., 2005; Trabucho Alexandre et al., 2011; Coccioni et al., 2014; Sabatino et al., 2015). The Kilian sub-event also exhibits a short-term negative carbon isotope excursion above the high carbon isotope records of the Jacob sub-event (Herrle et al., 2004; Coccioni et al., 2014). In the western Tethys and the eastern Pacific, the Kilian sub-event is characterized by a negative $\delta^{13}\text{C}_{\text{carb}}$ excursion reaching ~1‰ (Sabatino et al., 2015; Matsumoto et al. 2020) and a large negative $\delta^{13}\text{C}_{\text{org}}$ excursion reaching -26.3‰–25.8‰ (Navarro-Ramirez et al., 2015; Sabatino et al., 2015). In the eastern North Atlantic (DSDP Site 545, Mazagan Plateau), the Kilian sub-event shows a distinct negative carbon isotope excursion ranging from ~2‰ prior to the organic-rich interval to an average value of 0.75‰ during the sub-event, and then a gradual return to carbon isotopic values of ~1.2‰ at its termination (e.g., Herrle, 2002; Herrle et al., 2004; Friedrich et al., 2005; Trabucho Alexandre et al., 2011). In terrestrial records close to the western Pacific in southeastern China, the Kilian sub-event is expressed as a negative excursion with an average $\delta^{13}\text{C}_{\text{org}}$ value of -26.1‰ occurring the 44.4–44.7 m interval in the Shipu section and an average $\delta^{13}\text{C}_{\text{org}}$ value of -27.0‰ in the Chong'an section (Hu et al., 2014).

In the early Albian Fuxin Basin, from the bottom to the top the first interval of negative $\delta^{13}\text{C}_{\text{org}}$ excursion decreases from -26.1‰ to -27‰, and then back to -25.6‰ (Fig. 9). Amongst these, the peak value of the negative excursion corresponds with high TOC values up to 4.76% (Xu et al., 2022). Carbon isotopic records during the early Albian are the first distinctly

negative $\delta^{13}\text{C}_{\text{org}}$ excursion above the top of the positive $\delta^{13}\text{C}_{\text{org}}$ excursion, which coincides with the characteristics of the Kilian sub-event, a short negative excursion above the positive excursion in the carbon isotope record of the Jacob sub-event (Herrle et al., 2004). In addition, the age of the first negative excursion interval is younger than 112.6 ± 1.7 Ma according to the zircon U-Pb dating analysis (Xu et al., 2022), which could be regarded as the Kilian sub-event equivalent.

5.5.3 Recognition of the Paquier sub-event

The Paquier sub-event is the organic-rich expression of the third sub-event of OAE 1b (Coccioni et al., 2014). In western Tethys and western North Atlantic, the Paquier sub-event is 0.25–1.63 m thick and has TOC contents up to 8–12.3% (e.g., Herrle, 2002; Huber et al. 2011; Coccioni et al., 2014; Sabatino et al., 2015; Matsumoto et al. 2020). The Paquier sub-event is defined by a negative excursion in both marine carbonate and organic matter carbon isotope records (e.g., Erbacher et al., 2001; Herrle et al., 2004; Tsikos et al., 2004). In Tethys and the eastern Pacific, the Paquier sub-event commences with an abrupt negative $\delta^{13}\text{C}_{\text{carb}}$ shift reaching values as low as -0.68‰ – -2.2‰ , whereas $\delta^{13}\text{C}_{\text{org}}$ values exhibit a gradual negative shift reaching -27‰ (e.g., Coccioni et al., 2014; Sabatino et al., 2015; Navarro-Ramirez et al., 2015; Li et al., 2016). In terrestrial records of the western Pacific in southeastern China, the Paquier sub-event displays the strongest negative excursion with a $\delta^{13}\text{C}_{\text{org}}$ peak value of -27.8‰ in the Shipu section, and an average $\delta^{13}\text{C}_{\text{org}}$ value of -27.9‰ in the Chong'an section (Hu et al., 2014). In terrestrial settings close to eastern Tethys in northwestern China, the Paquier event occurs from 142.2 m–166.8 m in the Hanxiagou section from the Jiuquan Basin and exhibits a strong negative $\delta^{13}\text{C}_{\text{org}}$ excursion from -27‰ to -21.7‰ representing an $\sim 5\text{‰}$ change (Zhao et al., 2022).

In the study area, the second interval of negative $\delta^{13}\text{C}_{\text{org}}$ shift from the bottom of the early Albian decreases from -24.8‰ to -26.2‰ , followed by a positive $\delta^{13}\text{C}_{\text{org}}$ excursion with $\delta^{13}\text{C}_{\text{org}}$ values up to -24.9‰ (Fig. 9; Xu et al., 2022). The magnitude of the negative excursion (1.4‰) in the present study closely matches those in terrestrial records ($\sim 1.5\text{‰}$) from the Paquier sub-event, including evidence from fossil wood in Japan (Ando et al., 2007), palustrine nodules from the USA (Ludvigson et al., 2010), and terrestrial organic matter from southeastern China

(Hu et al., 2014). High resolution carbon isotope records from the Vocontian Basin show that the Paquier sub-event follows after the Kilian sub-event and has a carbon isotope record comprising a short negative excursion after a brief recovery above the Kilian sub-event (Fig. 9; Herrle et al., 2004). A similar negative $\delta^{13}\text{C}_{\text{org}}$ excursion in the early Albian Fuxin Basin suggests that it represents the counterpart of the Paquier sub-event.

5.5.4 Recognition of the Leenhardt sub-event

The Leenhardt sub-event is the organic-rich expression of the fourth sub-event of OAE 1b and has been documented in many regions of the world (Coccioni et al., 2014; Navarro-Ramirez et al., 2015; Li et al., 2016). In western Tethys, the Leenhardt sub-event is 29 cm–92 cm thick with TOC contents of 0.95–3% (Herrle, 2002; Coccioni et al., 2014; Sabatino et al., 2015). In Tethys and the eastern Pacific, the Leenhardt sub-event is characterized by a negative $\delta^{13}\text{C}_{\text{carb}}$ excursion reaching -0.1‰–1‰ with negative $\delta^{13}\text{C}_{\text{org}}$ excursion values as low as -28‰ (Coccioni et al., 2014; Navarro-Ramirez et al., 2015; Li et al., 2016). In terrestrial records close to the western Pacific in southeastern China, the Leenhardt sub-event shows a relatively weak negative $\delta^{13}\text{C}_{\text{org}}$ excursion with an average $\delta^{13}\text{C}_{\text{org}}$ value of -27.6‰ in the Chong'an section (Hu et al., 2014). In terrestrial records near eastern Tethys from northwestern China, $\delta^{13}\text{C}_{\text{org}}$ values decrease from -26.1‰ to -22.8‰ in the 228.3 m–236.3 m interval of the Hanxiagou section in the Jiuquan Basin (Zhao et al., 2022).

In the early Albian Fuxin Basin, from the bottom to the top, the third interval of negative $\delta^{13}\text{C}_{\text{org}}$ excursion decreases from -25.7‰ to -26.6‰, and then returns back to -25.1‰ at its termination (Xu et al., 2022). The magnitude of the negative excursion (1.5‰) is similar to those in the eastern Pacific Andean Basin (Navarro-Ramirez et al., 2015) and the western North Atlantic (ODP site 1049 off northern Florida, Blake Nose escarpment; Huber et al., 2011), but is higher than those of hemipelagic and platform carbonates in Tethys, such as from the Umbria-Marche Basin (Coccioni et al., 2014) and the Bangbu section in southern Tibet, China (Li et al., 2016). The negative $\delta^{13}\text{C}_{\text{org}}$ excursion with a peak value up to -26.6‰ is comparable to that of terrestrial records close to the western Pacific from southeastern China (Hu et al., 2014) and that of organic matter in the eastern Pacific Andean Basin (Navarro-Ramirez et al., 2015). Therefore, we conclude that this negative $\delta^{13}\text{C}_{\text{org}}$ shift from the early Albian Fuxin Basin

most likely represents the Leenhardt sub-event.

In the study area, four sharp, short-term negative $\delta^{13}\text{C}_{\text{org}}$ excursions occur during the late Aptian to early Albian and each corresponds with relatively high TOC values. Furthermore, these correlate well stratigraphically with the Jacob, Kilian, Paquier and Leenhardt sub-events of OAE 1b on the basis of zircon U-Pb age and changing trends and magnitudes of carbon isotope excursions. Based on carbon isotope chemostratigraphy, the sub-events of OAE 1b in the Fuxin Basin can therefore be correlated with six representative research cases including western Tethys, eastern Pacific, western North Atlantic and China (Fig. 9). This comparative analysis indicates that OAE 1b has a global signature and is not only expressed in marine settings but also can be recognized from the terrestrial record.

In the Fuxin Basin, mudstone samples in units A and B have seemingly circumvented the normal thermal history, because of the influence of diabase intrusion on the sedimentary strata at the bottom of the Shapai Formation (Zhang et al., 2003; Zhu et al., 2007). Therefore, we abandoned the analysis of wildfire events in units A and B. Three short-term increases of inertinite content and inertinite reflectance correspond to three negative $\delta^{13}\text{C}_{\text{org}}$ excursions and relatively high TOC values during the early Albian interval (Fig. 10). In the study area, the resulting estimates of inertinite content and inertinite reflectance provide evidence for enhanced continental wildfires during the Kilian, Paquier and Leenhardt sub-events of the OAE 1b (Fig. 10).

The widespread occurrences of wildfires depend on a combination of factors, such as flammable fuel accumulation, atmospheric $p\text{O}_2$ level, moisture content and ignition mechanism (Bond et al. 2010; Glasspool et al., 2015). The lush Fuxin flora in western Liaoning region during the late Albian–Aptian interval (Deng et al. 2012), would have provided an appropriate source of fuel. The relatively humid palaeoclimate in the early Albian (Xu et al., 2020a) would have reduced the likelihood of wildfire. However, the high $p\text{O}_2$ level of ~25% estimated in the early Albian might render vegetation with relatively high moisture more susceptible to combustion (Glasspool et al., 2015). Five potential sources (apart from human activity) of triggering ignition include lightning strikes, volcanic eruptions, meteor strikes, sparks from rock falls and spontaneous combustion (Belcher et al., 2010; Glasspool et al., 2015). Abundant local volcanic eruptions occurred in the western Liaoning region during the Lower Cretaceous

(Cai et al., 2010), which may have acted as the main source of ignition for wildfires.

Continental wildfires destroy land surface vegetation systems and soil structure, which increase soil erosion by continental chemical weathering and transfer of land materials (e.g., minerals, plant residues, charcoal and nutrient elements) into lacustrine and marine environments (Algeo and Ingall, 2007; Brown et al. 2012; Glasspool et al., 2015) contributing to eutrophication and anoxia in lacustrine and in contemporaneous oceanic systems (Brown et al. 2012; Yan et al., 2019; Xu et al., 2020a, 2022). In the study area, the high inertinite contents show that wildfires prevailed in northeastern China during the Lower Cretaceous. In addition, the vertical variation patterns of inertinite content and inertinite reflectance indicate short-term increasing trends of wildfire activity during the Kilian, Paquier and Leenhardt sub-events of the Albian OAE 1b (Fig. 10). Chemical weathering indices have been used to quantitatively track secular variation in chemical weathering intensity, with implications for palaeoclimate reconstruction (Nesbitt and Young, 1982; Fedo et al., 1995; Xu et al., 2018; Lu et al., 2020; Xu et al., 2020a; Gao et al., 2021). Various chemical weathering indices were compiled to illuminate the chemical weathering trend in the Fuxin Basin during the Lower Cretaceous, including the Chemical Index of Alteration (CIA; Nesbitt and Young, 1982), Mafic Index of Alteration for Oxidative weathering environments ($MIA_{(O)}$; Babechuk et al., 2014) and Weathering Index of Parker (WIP; Parker, 1970). The degree of chemical weathering calculated using the chemical weathering indices (CIA, WIP and $MIA_{(O)}$) show an increasing trend during the early Albian OAE 1b interval (Xu et al., 2020a). In the study area, sandstones associated with abundant charcoal fragments have been identified in the Fuxin Basin (Fig. 5a and 5c), which probably represents a post-fire erosion deposit. These sandstones contain charcoals and may be related to increased soil erosion after wildfires. As the result of frequent wildfire activity and intensified chemical weathering, abundant nutrients and organic matter may be transported from continents into lakes where nutrients might increase productivity in surface waters. Transported tree trunk fossils were identified in lacustrine environments of the early Albian (Fig. 5b, 5g and 5h) providing evidence that terrestrial plants were flushed into lakes. Many fossil charcoals identified in lacustrine mudstone in the DY-1 borehole (Fig. 5d, 5e and 5f) may also demonstrate that high flux of nutrients and organic matter produced by increasing wildfire activity and chemical weathering were flushed into lakes through surface

runoff. Ultimately, decaying organic matter in surface waters, including terrestrial plants and lacustrine plankton, consumed oxygen during downward passage through the water column, which in turn led to anoxia in lakes (Fig. 12). This unit correlates with the early Albian OAE 1b, inferring that frequent wildfire activity at this time promoted high nutrient levels and organic matter that were flushed into marine systems, triggering contemporaneous ocean anoxic event. In this context, many organisms gradually died and organic matter was buried and preserved with an expansion of the oxygen-minimum zone. These results support previous work which proposed that increased wildfires activity stimulated eutrophication and anoxia in lakes and oceans and ultimately organic carbon burial (Brown et al., 2012; Yan et al., 2019; Boudinot and Sepúlveda, 2020).

6. Conclusions

(1) High levels of inertinite contents and PAHs in mudstone samples provide evidence for widespread wildfires during the early Albian. The main types of wildfires in the early Albian were ground and surface fires, and the frequency of surface fires was high. Inferred pO_2 levels in the early Albian atmosphere, as estimated from inertinite contents, were ~25%, which is much higher than the minimum needed for sustained combustion. Sufficient fuel accumulation and frequent surface fires under high pO_2 levels might have contributed towards the evolution of early angiosperms in Lower Cretaceous environments.

(2) Wildfires destroyed vegetation cover and soil structure in the Fuxin Basin during the early Albian, which enhanced post-fire erosion under the conditions of intensified continental weathering. Post-fire erosion and vegetation destruction may have promoted elevated levels of nutrients and organic matter that were flushed into lakes and thereby contributed to eutrophication and anoxia in lacustrine and contemporaneous oceanic systems. These corresponds to the Kilian, Paquier and Leenhardt sub-events of the early Albian OAE 1b and suggest a temporal linkage between terrestrial and marine environmental perturbations.

Declaration of Competing Interest

The authors declare that they have no known competing financial interests or personal relationships that could have appeared to influence the work reported in this paper.

Acknowledgments

This study was supported by the Yue Qi Scholar Project of China University of Mining and Technology (Beijing), the National Natural Science Foundation of China (41572090; 42002128) and Shandong Key Laboratory of Depositional Mineralization & Sedimentary Mineral, Shandong University of Science and Technology (DMSM20190015). We thank the two anonymous reviewers for the insightful and helpful reviews.

References

- Algeo, T.J., Ingall, E., 2007. Sedimentary C_{org} : P ratios, paleocean ventilation, and Phanerozoic atmospheric pO_2 . *Palaeogeogr. Palaeoclimatol. Palaeoecol.* 256 (3–4), 130–155.
<https://doi.org/10.1016/j.palaeo.2007.02.029>.
- Ando, A., Kakegawa, T., 2007. Carbon isotope records of terrestrial organic matter and occurrence of planktonic foraminifera from the Albian stage of Hokkaido, Japan: ocean-atmosphere $\delta^{13}C$ trends and chronostratigraphic implications. *Palaios* 22, 417–432.
<http://dx.doi.org/10.2110/palo.2005.p05-104r>.
- Arvidson, R.S., Mackenzie, F.T., Guidry, M., 2006. MAGic: A Phanerozoic model for the geochemical cycling of major rock-forming components. *Am. J. Sci.* 306(3), 135–190.
<https://doi.org/10.2475/ajs.306.3.135>.
- Babechuk, M.G., Widdowson, M., Kamber, B.S. 2014. Quantifying chemical weathering intensity and trace element release from two contrasting basalt profiles, Deccan Traps, India. *Chem. Geol.* 363, 56–75. <https://doi.org/10.1016/j.chemgeo.2013.10.027>.
- Baker, S.J., Hesselbo, S.P., Lenton, T.M., Duarte, L.V., Belcher, C.M., 2017. Charcoal evidence that rising atmospheric oxygen terminated Early Jurassic ocean anoxia. *Nat. Commun.* 8, 15018. <https://doi.org/10.1038/ncomms15018>.
- Barral, A., Gomez, B., Fourel, F., Daviero-Gomez, V., Lécuyer, C., 2017. CO_2 and temperature decoupling at the million-year scale during the Cretaceous Greenhouse. *Sci. Rep.* 7, 8310. <https://doi.org/10.1038/s41598-017-08234-0>.
- Belcher, C.M., McElwain, J.C., 2008. Limits for combustion in low O_2 redefine paleoatmospheric predictions for the Mesozoic. *Science* 321(5893), 1197–200.

750 <https://doi.org/10.1126/science.1160978>.

751 Belcher, C.M., Hudspeth, V.A., 2017. Changes to Cretaceous surface fire behaviour influenced
 752 the spread of the early angiosperms. *New Phytol.* 213, 1521–1532.
 753 <https://doi.org/10.1111/nph.14264>.

754 Belcher, C.M., Mills, B.J.W., Vitali¹, R., Baker¹, S.J., Lenton, T.M., Watson, A.J., 2021. The
 755 rise of angiosperms strengthened fire feedbacks and improved the regulation of
 756 atmospheric oxygen. *Nat. Commun.* 12, 503. [https://doi.org/10.1038/s41467-020-20772-](https://doi.org/10.1038/s41467-020-20772-2)
 757 2.

758 Belcher, C.M., Yearsley, J.M., Hadden, R.M., McElwain, J.C., Rein, G., 2010. Baseline
 759 intrinsic flammability of Earth’s ecosystems estimated from paleoatmospheric oxygen
 760 over the past 350 million years. *PNAS* 107(52), 22448–22453.
 761 <https://doi.org/10.1073/pnas.1011974107>.

762 Berendse, F., Scheffer, M., 2009. The angiosperm radiation revisited, an ecological explanation
 763 for Darwin’s ‘abominable mystery’. *Ecol. Lett.* 12, 865–872.
 764 <https://doi.org/10.1111/j.1461-0248.2009.01342.x>.

765 Bergman, N.M., 2004. COPSE: A new model of biogeochemical cycling over Phanerozoic
 766 time. *Am. J. Sci.* 304(5), 397–437. <https://doi.org/10.2475/ajs.304.5.397>.

767 Berner, R.A., 2009. Phanerozoic atmospheric oxygen: New results using the GEOCARBSULF
 768 model. *Am. J. Sci.* 309(7), 603–606. <https://doi.org/10.2475/07.2009.03>.

769 Boudinot, F.G., Sepúlveda, J., 2020. Marine organic carbon burial increased forest fire
 770 frequency during Oceanic Anoxic Event 2. *Nat. Geosci.* 13, 693–698.
 771 <https://doi.org/10.1038/s41561-020-0633-y>.

772 Bond, W.J., Keeley, J.E., 2005. Fire as a global ‘herbivore’: the ecology and evolution of
 773 flammable ecosystems. *Trends Ecol. Evol.* 20(7), 387–394.
 774 <https://doi.org/10.1016/j.tree.2005.04.025>.

775 Bond, W.J., Scott, A.C., 2010. Fire and the spread of flowering plants in the Cretaceous. *New*
 776 *Phytol.* 188, 1137–1150. <https://doi.org/10.1111/j.1469-8137.2010.03418.x>.

777 Brenner, G.J., 1976. Middle Cretaceous floral provinces and early migrations of angiosperms.
 778 In: Beck, C.B. (Ed.), *Origin and Early Evolution of Angiosperms*. Columbia University
 779 Press, New York, USA, pp. 23–47.

780 Brodribb, T.J., Feild, T.S., 2010. Leaf hydraulic evolution led a surge in leaf photosynthetic
 781 capacity during early angiosperm diversification. *Ecol. Lett.* 13, 175–183.
 782 <https://doi.org/10.1111/j.1461-0248.2009.01410.x>.

783 Brown, S.A.E., Scott, A.C., Glasspool, I.J., Collinson, M.E., 2012. Cretaceous wildfires and
 784 their impact on the Earth system. *Cretaceous Res.* 36, 162–190.
 785 <https://doi.org/10.1016/j.cretres.2012.02.008>.

786 Bustin, R.M., Guo, Y., 1999. Abrupt changes (jumps) in reflectance values and chemical
 787 compositions of artificial charcoals and inertinite in coals. *Int. J. Coal Geol.* 38, 237–260.
 788 [https://doi.org/10.1016/S0166-5162\(98\)00025-1](https://doi.org/10.1016/S0166-5162(98)00025-1).

789 Cai, H.A., Li, B.F., Shao, L.Y., Xu, D.B., Shao, K., Zhou, Y.Y., 2011. Sedimentary
 790 environments and coal accumulation patterns of the Lower Cretaceous Shahai Formation
 791 in Fuxin Basin, Liaoning Province. *J. Palaeogeogr.* 13 (5), 481–491 (in Chinese with
 792 English abstract).

793 Cai, H.A., Xu, D.B., Li, B.F., Shao, L.Y., 2010. A study on Early Cretaceous volcanic effusion
 794 periods and isotope chronology in western Liaoning. *Coal Geol. Explor.* 22 (12), 1–6 (in
 795 Chinese with English abstract).

796 Chefetz, B., Deshmukh, A.P., Hatcher, P.G., Guthrie, E.A., 2000. Pyrene sorption by natural
 797 organic matter. *Environ. Sci. Technol.* 34(14), 2925–2930.
 798 <https://doi.org/10.1021/es9912877>.

799 Chen, F., Meng, X.Y., Ren, S.Q., Wu, C.L., 1988. The Early Cretaceous flora of Fuxin Basin
 800 and Tiefa Basin, Liaoning Province. Geological Publishing House, Beijing, pp. 1–180. (in
 801 Chinese).

802 Chen, F., Yang, G.X., Zhou, H.Q., 1981. Early Cretaceous flora in Fuxin Basin, Liaoning
 803 Province. *J. Earth Sci. (Chinese Ed.)* 6(2), 39–55. (in Chinese with English abstract).

804 Coccioni, R., Sabatino, N., Frontalini, F., Gardin, S., Sideri, M., Sprovieri, M., 2014. The
 805 neglected history of Oceanic Anoxic Event 1b: insights and new data from the Poggio le
 806 Guaine section (Umbria-Marche Basin). *Stratigraphy* 11(3–4), 245–282.

807 Coiro, M., Doyle, J.A., Hilton, J., 2019. How deep is the conflict between molecular and fossil
 808 evidence on the age of angiosperms? *New Phytol.* 223, 83–89.
 809 <https://doi.org/10.1111/nph.15708>.

810 Couper, R.A., 1958. British Mesozoic microspores and pollen grains. *Palaeontographica*
811 *Abteilung B* 103, 75–179.

812 Deng, S.H., Chen, F., 2001. The Early Cretaceous Filicopsida from Northeast China.
813 Geological Publishing House, Beijing, pp. 1–249 (in Chinese).

814 Deng, S.H., Lu, Y.Z., Fan, R., Li, X., Fang, L.H., Liu, L., 2012. Cretaceous floras and
815 biostratigraphy of China. *J. Stratigr.* 36(2), 241–265.

816 Denis, E.H. Toney, J.L., Taroza, R., Scott Anderson, R., Roach, L.D. Huang, Y.S., 2012.
817 Polycyclic aromatic hydrocarbons (PAHs) in lake sediments record historic fire events:
818 Validation using HPLC-fluorescence detection. *Org. Geochem.* 45, 7–17.
819 <https://doi.org/10.1016/j.orggeochem.2012.01.005>.

820 Diessel, C.F.K., 2010. The stratigraphic distribution of inertinite. *Int. J. Coal Geol.* 81, 251–
821 268. <https://doi.org/10.1016/j.coal.2009.04.004>.

822 Erbacher, J., Huber, B.T., Norris, R.D., Markey, M., 2001. Increased thermohaline stratification
823 as a possible cause for an ocean anoxic event in the Cretaceous period. *Nature* 409, 325–
824 327. <https://doi.org/10.1038/35053041>.

825 Fedo, C.M., Nesbitt, H.W., Young, G.M., 1995. Unravelling the effects of potassium
826 metasomatism in sedimentary rocks and paleosols, with implications for paleoweathering
827 conditions and provenance. *Geology* 23(10), 921–924.

828 Feild, T.S., Brodribb, T.J., Iglesias, A., Chatelet, D.S., Baresch, A., Jr., G.R.U., Gomez, B.,
829 Mohr, B.A.R., Coiffard, C., Kvacek, J., Jaramillo, C., 2011. Fossil evidence for
830 Cretaceous escalation in angiosperm leaf vein evolution. *PNAS* 108(20), 8363–8366.
831 <https://doi.org/10.1073/pnas.1014456108>.

832 Finkelstein, D.B., Pratt, L.M., Curtin, T.M., Brassell, S.C., 2005. Wildfires and seasonal aridity
833 recorded in Late Cretaceous strata from south-eastern Arizona, USA. *Sedimentology* 52,
834 587–599. <https://doi.org/10.1111/j.1365-3091.2005.00712.x>.

835 Friis, E.M., Pedersen, K.R., Crane, P.R., 2010. Cretaceous diversification of angiosperms in the
836 western part of the Iberian Peninsula. *Rev. Palaeobot. Palyno.* 162, 341–361.
837 <https://doi.org/10.1016/j.revpalbo.2009.11.009>.

838 Friedrich, O., Nishi, H., Pross, J., Schmiedl, G., Hemleben, C., 2005. Millennial- to Centennial-
839 Scale Interruptions of the Oceanic Anoxic Event 1b (Early Albian, mid-Cretaceous)

840 Inferred from Benthic Repopulation Events. *Palaios* 20, 64–77.
841 <https://doi.org/10.2110/palo.2003.p03-75>.

842 Gao, Y., Ibarra, D.E., Caves Rugenstein, J.K., Chen, J.Q., Kukla, T., Methner, K., Gao, Y.F.,
843 Huang, H., Lin, Z.P., Zhang, L.M., Xi, D.P., Wu, H.C., Carroll, A.R., Graham, S.A.,
844 Chamberlain, C.P., Wang, C.S., 2021. Terrestrial climate in mid-latitude East Asia from
845 the latest Cretaceous to the earliest Paleogene: A multiproxy record from the Songliao
846 Basin in northeastern China. *Earth-Science Reviews* 216, 103572.
847 <https://doi.org/10.1016/j.earscirev.2021.103572>.

848 Galloway, J.M., Sweet, A.R., Pugh, A., Schröder-Adams, C.J., Swindles, G.T., Haggart, J.W.,
849 Embry, A.F., 2012. Correlating middle Cretaceous palynological records from the
850 Canadian High Arctic based on a section from the Sverdrup Basin and samples from the
851 Eclipse Trough. *Palynology* 36, 277–302. <https://doi.org/10.1080/01916122.2012.670411>.

852 Glasspool, I.J., Edwards, D., Axe, L., 2004. Charcoal in the Silurian as evidence for the earliest
853 wildfire. *Geology* 32(5), 381–383. <https://doi.org/10.1130/G20363.1>.

854 Glasspool, I.J., Scott, A.C., 2010. Phanerozoic concentrations of atmospheric oxygen
855 reconstructed from sedimentary charcoal. *Nat. Geosci.* 3, 627–630.
856 <https://doi.org/10.1038/NGEO923>.

857 Glasspool, I.J., Scott, A.C., Waltham, D., Pronina, N., Shao, L.Y., 2015. The impact of fire on
858 the Late Paleozoic Earth system. *Front. Plant Sci.* 6, 756.
859 <https://doi.org/10.3389/fpls.2015.00756>.

860 Grice, K., Nabbefeld, B., Maslen, E., 2007. Source and significance of selected polycyclic
861 aromatic hydrocarbons in sediments (Hovea-3 well, Perth Basin, Western Australia)
862 spanning the Permian–Triassic boundary. *Org. Geochem.* 38, 1795–1803.
863 <https://doi.org/10.1016/j.orggeochem.2007.07.001>.

864 Guo, Z.Y., 1988. Relationship between alluvial fan-delta depositional system and coal
865 accumulation of Shahai Formation in Fuxin Basin. *Coal Geol. Explor.* 16(4), 2–7. (in
866 Chinese).

867 Handoh, I.C., Lenton, T.M., 2003. Periodic mid-Cretaceous oceanic anoxic events linked by
868 oscillations of the phosphorus and oxygen biogeochemical cycles. *Global Biogeochem.*
869 *Cy.* 17(4), 1092. <https://doi.org/10.1029/2003GB002039>.

870 Harland, M., Francis, J.E., Brentnall, S.J., Beerling, D.J., 2007. Cretaceous (Albian–Aptian)
871 conifer wood from Northern Hemisphere high latitudes: Forest composition and
872 palaeoclimate. *Rev. Palaeobot. Palyno.* 143, 167–196.
873 <https://doi.org/10.1016/j.revpalbo.2006.07.005>.

874 Haworth, M., Hesselbo, S.P., McElwain, J.C., Robinson, S.A., Brunt, J.W., 2005. Mid-
875 Cretaceous $p\text{CO}_2$ based on stomata of the extinct conifer *Pseudofrenelopsis*
876 (Cheirolepidiaceae). *Geology* 33(9), 749–752. <https://doi.org/10.1130/G21736.1>.

877 He, H.Y., Wang, X.L., Zhou, Z.H., Wang, F., Boven, A., Shi, G.H., Zhu, R.X., 2004. Timing
878 of the Jiufotang Formation (Jehol Group) in Liaoning, northeastern China, and its
879 implications. *Geophys. Res. Lett.* 31, 261–268. <https://doi.org/10.1029/2004GL019790>.

880 He, T., Lamont, B.B., 2018. Baptism by fire: the pivotal role of ancient conflagrations in
881 evolution of the Earth’s flora. *Natl. Sci. Rev.* 5, 237–254.
882 <https://doi.org/10.1093/nsr/nwx041>.

883 Heimhofer, U., Hochuli, P.A., Herrle, J.O., Weissert, H., 2006. Contrasting origins of Early
884 Cretaceous black shales in the Vocontian basin: Evidence from palynological and
885 calcareous nannofossil records. *Palaeogeogr. Palaeoclimatol. Palaeoecol.* 235, 93–109.
886 <https://doi.org/10.1016/j.palaeo.2005.09.025>.

887 Herrle, J.O., 2002. Mid-Cretaceous paleoceanographic and paleoclimatologic implications on
888 black shale formation of the Vocontian Basin and Atlantic: evidence from calcareous
889 nannofossils and stable isotopes. *Tübinger Mikropaläontologische Mitteilungen* 27, 1–
890 114.

891 Herrle, J.O., Kößler, P., Friedrich, O., Erlenkeuser, H., Hemleben, C., 2004. High-resolution
892 carbon isotope records of the Aptian to Lower Albian from SE France and the Mazagan
893 Plateau (DSDP Site 545): a stratigraphic tool for paleoceanographic and paleobiologic
894 reconstruction. *Earth Planet Sci. Lett.* 218(1), 149–161. [https://doi.org/10.1016/S0012-](https://doi.org/10.1016/S0012-821X(03)00646-0)
895 [821X\(03\)00646-0](https://doi.org/10.1016/S0012-821X(03)00646-0).

896 Herrle, J.O., Schroder-Adams, C.J., Davis, W., Pugh, A.T., Galloway, J.M., Fath, J., 2015. Mid-
897 Cretaceous High Arctic stratigraphy, climate, and Oceanic Anoxic Events. *Geology* 43(5),
898 403–406. <https://doi.org/10.1130/G36439.1>.

899 Hilton, J., Bateman, R.M., 2006. Pteridosperms are the backbone of seed–plant phylogeny.

Journal of the Torrey Botanical Society 133, 119–168. [https://doi.org/10.3159/1095-5674\(2006\)133\[119:PATBOS\]2.0.CO;2](https://doi.org/10.3159/1095-5674(2006)133[119:PATBOS]2.0.CO;2).

Hou, H.H., Shao, L.Y., Tang, Y., Li, Y.N., Liang, G.D., Xin, Y.L., Zhang, J.Q., 2020. Coal seam correlation in terrestrial basins by sequence stratigraphy and its implications for palaeoclimate and palaeoenvironment. *J. Earth Sci.* <https://doi.org/10.1007/s12583-020-1069-4>.

Hower, J.C., O'Keefe, J.M.K., Wagner, N.J., Dai, S.F., Wang, X.B., Xue, W.F., 2013. An investigation of Wulantuga coal (Cretaceous, Inner Mongolia) macerals: Paleopathology of faunal and fungal invasions into wood and the recognizable clues for their activity. *Int. J. Coal Geol.* 114(30), 44–53. <https://doi.org/10.1016/j.coal.2013.04.005>.

Hong, S.K., Lee, Y.I., 2012. Evaluation of atmospheric carbon dioxide concentrations during the Cretaceous. *Earth Planet. Sci. Lett.* 327–328, 23–28. <https://doi.org/10.1016/j.epsl.2012.01.014>.

Hu, G., Hu, W., Cao, J., Yao, S., Liu, W., Zhou, Z., 2014. Fluctuation of organic carbon isotopes of the Lower Cretaceous in coastal southeastern China: Terrestrial response to the Oceanic Anoxic Events (OAE 1b). *Palaeogeogr. Palaeoclimatol. Palaeoecol.* 399, 352–362. <http://dx.doi.org/10.1016/j.palaeo.2014.01.027>.

Huang, J.G., Bergeron, Y., Denneler, B., Berninger, F., Tardif, J., 2007. Response of forest trees to increased atmospheric CO₂. *Crit. Rev. Plant Sci.* 26, 265–283. <https://doi.org/10.1080/07352680701626978>.

Huber, B.T., Macleod, K.G., Gröcke, D.R., Kucera, M., 2011. Paleotemperature and paleosalinity inferences and chemostratigraphy across the Aptian/Albian boundary in the subtropical North Atlantic. *Paleoceanography* 26, PA4221. <http://dx.doi.org/10.1029/2011PA002178>.

Jasper, A., Agnihotri, D., Tewari, R., Spiekermann, R., Pires, E.F., Rosa, Á.A.S.D., Uhl, D., 2016. Fires in the mire: repeated fire events in Early Permian ‘peat forming’ vegetation of India. *Geol. J.* 52(6), 955–969. <http://dx.doi.org/10.1002/gj.2860>.

Jenkyns, H.C., 2010. Geochemistry of oceanic anoxic events. *Geochem. Geophys. Geosy.* 11(3), 1–30. <http://dx.doi.org/10.1029/2009GC002788>.

Jiang, C., Alexander, R., Kagi, R.I., Murray, A.P., 1998. Polycyclic aromatic hydrocarbons in

930 ancient sediments and their relationships to palaeoclimate. *Org. Geochem.* 29(5-7), 1721–
 931 1735. [http://dx.doi.org/10.1016/S0146-6380\(98\)00083-7](http://dx.doi.org/10.1016/S0146-6380(98)00083-7).

932 Jones, T.P., Chaloner, W.G., 1991. Fossil charcoal, its recognition and palaeoatmospheric
 933 significance. *Palaeogeogr. Palaeoclimatol. Palaeoecol.* 97(1–2), 39–50.
 934 [https://doi.org/10.1016/0031-0182\(91\)90180-Y](https://doi.org/10.1016/0031-0182(91)90180-Y).

935 Jones, T.P., Scott, A.C., Cope, M., 1991. Reflectance measurements and the temperature of
 936 formation of modern charcoals and implications for studies of fusain. *Bulletin de la*
 937 *Société Géologique de France* 162(2), 193–200.

938 Jones, T.P., 1994. New morphological and chemical evidence supporting a wildfire origin for
 939 fusain from comparisons with modern charcoal. In: Collinson, M. and Scott, A.C. (Eds.),
 940 *Studies in Palaeobotany and Palynology in Honour of Professor W. G. Chaloner, F.R.S.,*
 941 *Special Papers in Palaeontology*, vol. 49. Palaeontological Association, London, pp. 113–
 942 123.

943 Jones, T.P., 1996. A fire-related origin for fusain: comparisons with the physicochemical
 944 characteristics of laboratory produced charcoal. *Neues Jahrbuch für Geologie und*
 945 *Paläontologie - Abhandlungen* 202(2), 159–168.
 946 <https://doi.org/10.1127/njgpa/202/1996/159>.

947 Jones, T.P., 1997. Fusain in Late Jurassic sediments from Witch Ground Graben, North Sea,
 948 U.K. *Mededelingen Nederlands Instituut voor Toegepaste Geowetenschappen TNO* 58,
 949 93–103.

950 Kang, S.L., Shao, L.Y., Qin, L.Z., Li, S.X., Liu, J.S., Shen, W.C., Chen, X.D., Eriksson, K.A.,
 951 Zhou, Q.Y., 2020. Hydrocarbon generation potential and depositional setting of Eocene
 952 oil-prone coaly source rocks in the Xihu Sag, East China Sea Shelf Basin. *ACS Omega*
 953 5(50), 32267–32285. <https://dx.doi.org/10.1021/acsomega.0c04109>.

954 Korasidis, V.A., Wagstaff, B.E., Gallagher, S.J., Duddy, I.R., Tosolini, AMP., Cantrill, D.J.,
 955 Norvick, M.S., 2016. Early angiosperm diversification in the Albian of southeast
 956 Australia: implications for flowering plant radiation across eastern Gondwana. *Rev.*
 957 *Palaeobot. Palyno.* 232: 61–80. <https://doi.org/10.1016/j.revpalbo.2016.04.005>.

958 Leng, Q., Friis, E.M., 2003. *Sinocarpus decussates* gen. et sp. nov., a new angiosperm with
 959 basally syncarpous fruits from the Yixian Formation of Northeast China. *Plant Syst. Evol.*

241, 77–88.

Li, J.H., Jiang, H.F., 2013. Global palaeoplate reconstruction, lithofacies palaeogeography and paleoenvironmental atlas. Geological Publishing House, Beijing, pp. 1–127 (in Chinese).

Li, S.T., 1988. Fault basin analysis and coal accumulation. Geological Publishing House, Beijing, pp. 1–367. (in Chinese).

Li, X.H., Wei, Y.S., Li, Y.X., Zhang, C.K., 2016. Carbon isotope records of the early Albian oceanic anoxic event (OAE) 1b from eastern Tethys (southern Tibet, China). *Cretaceous Res.* 62, 109–121. <https://doi.org/10.1016/j.cretres.2015.08.015>.

Liu, J.Y., Wang, S.Y., Yin, J.H., 1992, Petroleum geological character of Fuxin Basin. *Oil Gas Geol.* 13(4), 450–457 (in Chinese with English abstract).

Liu, G.Q., Zhang, G., Li, X.D., Li, J., Peng, X.Z., Qi, S.H., 2005. Sedimentary record of polycyclic aromatic hydrocarbons in a sediment core from the Pearl River Estuary, South China. *Mar. Pollut. Bull.* 51, 912–921. <https://dx.doi.org/10.1016/j.marpolbul.2005.02.038>.

Liu, Z.Y., Selby, D., Hackley, P.C., Jeffrey Over, D., 2020. Evidence of wildfires and elevated atmospheric oxygen at the Frasnian–Famennian boundary in New York (USA): Implications for the Late Devonian mass extinction. *Geol. Soc. Am. Bull.* 132 (9-10), 2043–2054. <https://doi.org/10.1130/B35457.1>.

Lu, J., Zhou, K., Yang, M.F., Eley, Y., Shao, L.Y., Hilton, J., 2020. Terrestrial organic carbon isotopic composition ($\delta^{13}\text{C}_{\text{org}}$) and environmental perturbations linked to Early Jurassic volcanism: evidence from the Qinghai-Tibet Plateau of China. *Glob. Planet. Chang.* 195, 103331. <https://doi.org/10.1016/j.gloplacha.2020.103331>.

Lu, M., Ikejiri, T., Lu, Y.H., 2021. A synthesis of the Devonian wildfire record: Implications for paleogeography, fossil flora, and paleoclimate. *Palaeogeogr. Palaeoclimatol. Palaeoecol.* 571, 110321. <https://doi.org/10.1016/j.palaeo.2021.110321>.

Ludvigson, G.A., Joeckel, R.M., Gonzalez, L.A., Gulbranson, E.L., Rasbury, E.T., Hunt, G.J., Kirkland, J.I., Madsen, S., 2010. Correlation of Aptian–Albian carbon isotope excursions in continental strata of the Cretaceous foreland basin, eastern Utah, U.S.A. *J. Sed. Res.* 80, 955–974. <http://dx.doi.org/10.2110/jsr.2010.086>.

Marynowski, L., Kurkiewicz, S., Rakocinski, M., Simoneit, B.R.T., 2011. Effects of

990 weathering on organic matter: I. Changes in molecular composition of extractable organic
 991 compounds caused by paleoweathering of a Lower Carboniferous (Tournaisian) marine
 992 black shale. *Chem. Geol.* 285, 144–156. <https://dx.doi.org/10.1016/j.chemgeo.2011.04.001>.
 993 Marynowski, L., Simoneit, B.R.T., 2009. Widespread upper Triassic to Lower Jurassic wildfire
 994 records from Poland: Evidence from charcoal and pyrolytic polycyclic aromatic
 995 hydrocarbons. *Palaios* 24, 785–798. <https://dx.doi.org/10.2110/palo.2009.p09-044r>.
 996 Matsumoto, H., Kuroda, J., Coccioni, R., Frontalini, F., Sakai, S., Ogawa, N.O., Ohkouchi, N.,
 997 2020. Marine Os isotopic evidence for multiple volcanic episodes during Cretaceous
 998 Oceanic Anoxic Event 1b. *Sci. Rep.* 10, 12601. [https://doi.org/10.1038/s41598-020-](https://doi.org/10.1038/s41598-020-69505-x)
 999 69505-x.
 1000 Meng, Y., Liu, X.H., Lu, S.Y., Zhang, T.T., Jin, B.C., Wang, Q., Tang, Z.R., Liu, Y., Guo, X.H.,
 1001 Zhou, J.L., Xi, B.D., 2019. A review on occurrence and risk of polycyclic aromatic
 1002 hydrocarbons (PAHs) in lakes of China. *Sci. Total Environ.* 651, 2497–2506.
 1003 <https://doi.org/10.1016/j.scitotenv.2018.10.162>.
 1004 Mills, B.J.W., Belcher, C.M., Lenton, T.M., Newton, R.J., 2016. A modeling case for high
 1005 atmospheric oxygen concentrations during the Mesozoic and Cenozoic. *Geology*, 44(12),
 1006 1023–1026. <https://doi.org/10.1130/G38231.1>.
 1007 Moore, T.A., Moroeng, O.M., Shen, J., Esterle, J.S., Pausch, R.C., 2021. Using carbon isotopes
 1008 and organic composition to decipher climate and tectonics in the Early Cretaceous: An
 1009 example from the Hailar Basin, Inner Mongolia, China. *Cretaceous Res.* 118, 104674.
 1010 <https://doi.org/10.1016/j.cretres.2020.104674>.
 1011 Murchison, D.G., Raymond, A.C., 1989. Igneous activity and organic maturation in the
 1012 Midland Valley of Scotland. *Int. J. Coal Geol.* 14, 47–82. [https://doi.org/10.1016/0166-](https://doi.org/10.1016/0166-5162(89)90078-5)
 1013 5162(89)90078-5.
 1014 Navarro-Ramirez, J.P., Bodin, S., Heimhofer, U., Immenhauser, A., 2015. Record of Albian to
 1015 early Cenomanian environmental perturbation in the eastern sub-equatorial Pacific.
 1016 *Palaeogeogr. Palaeoclimatol. Palaeoecol.* 423, 122–137.
 1017 <http://dx.doi.org/10.1016/j.palaeo.2015.01.025>.
 1018 Nesbitt, H.W., Young, G.M., 1982. Early Proterozoic climates and plate motions inferred from
 1019 major element chemistry of lutites. *Nature* 299, 715–717.

1020 <https://doi.org/10.1038/299715a0>.

1021 Oakley, O., Falcon-Lang, H.J., 2009. Morphometric analysis of Cretaceous (Cenomanian)

1022 angiosperm woods from the Czech Republic. *Rev. Palaeobot. Palyno.* 153, 375–385.

1023 <https://doi.org/10.1016/j.revpalbo.2008.10.006>.

1024 Page, D.S., Boehm, P.D., Douglas, G.S., Bence, A.E., Burns, W.A., Mankiewicz, P.J., 1999.

1025 Pyrogenic polycyclic aromatic hydrocarbons in sediments record past human activity: A

1026 case study in Prince William Sound, Alaska. *Mar. Pollut. Bull.* 38(4), 247–260.

1027 [https://doi.org/10.1016/S0025-326X\(98\)00142-8](https://doi.org/10.1016/S0025-326X(98)00142-8).

1028 Parker, A. 1970. An index of weathering for silicate rocks. *Geol. Mag.* 107(6), 501–504.

1029 <https://doi.org/10.1017/S0016756800058581>.

1030 Petersen, H.I., Lindstrom, S., 2012. Synchronous wildfire activity rise and mire deforestation at

1031 the Triassic–Jurassic boundary. *PLOS ONE* 7(10), e47236.

1032 <https://doi.org/10.1371/journal.pone.0047236>.

1033 Royer, D.L., Miller, I.M., Peppe, D.J., Hickey, L.J., 2010. Leaf economic traits from fossils

1034 support a weedy habit for early angiosperms. *Am. J. Bot.* 97(3), 438–445.

1035 <https://doi.org/10.3732/ajb.0900290>.

1036 Sabatino, N., Coccioni, R., Manta, D.S., Baudin, F., Vallefucio, M., Traina, A., Sprovieri, M.,

1037 2015. High-resolution chemostratigraphy of the late Aptian-early Albian oceanic anoxic

1038 event (OAE 1b) from the Poggio le Guaine section (Umbria–Marche Basin, central Italy).

1039 *Palaeogeogr. Palaeoclimatol. Palaeoecol.* 426, 319–333.

1040 <https://doi.org/10.1016/j.palaeo.2015.03.009>.

1041 Scott, A.C., 2002. Coal petrology and the origin of coal macerals: a way ahead? *Int. J. Coal*

1042 *Geol.* 50, 119–134.

1043 Scott, A.C., 2010. Charcoal recognition, taphonomy and uses in palaeoenvironmental analysis.

1044 *Palaeogeogr. Palaeoclimatol. Palaeoecol.* 291, 11–39.

1045 <https://doi.org/10.1016/j.palaeo.2009.12.012>.

1046 Scott, A.C., Glasspool, I.J., 2006. The diversification of Paleozoic fire systems and fluctuations

1047 in atmospheric oxygen concentration. *PNAS* 103(29), 10861–10865.

1048 <https://doi.org/10.1073/pnas.0604090103>.

1049 Scott, A.C., Glasspool, I.J., 2007. Observations and experiments on the origin and formation of

1050 inertinite group macerals. *Int. J. Coal Geol.* 70, 53–66.
 1051 <https://doi.org/10.1016/j.coal.2006.02.009>.
 1052 Scott, A.C., Jones, T.P., 1994. The nature and influence of fire in Carboniferous ecosystems.
 1053 *Palaeogeogr. Palaeoclimatol. Palaeoecol.* 106, 91–112. [https://doi.org/10.1016/0031-](https://doi.org/10.1016/0031-0182(94)90005-1)
 1054 0182(94)90005-1.
 1055 Sender, L.M., Villanueva-Amadoz, U., Pons, D., Diez, J.B., Ferrer, J., 2014. Singular
 1056 taphonomic record of a wildfire event from middle Albian deposits of Escucha Formation
 1057 in northeastern of Spain. *Hist. Biol.* 27(3–4), 442–452.
 1058 <https://doi.org/10.1080/08912963.2014.895827>.
 1059 Shao, L.Y., Wang, H., Yu, X.H., Lu, J., Zhang, M.Q., 2012. Paleo-fires and atmospheric oxygen
 1060 levels in the latest Permian: evidence from maceral compositions of coals in Eastern
 1061 Yunnan, Southern China. *Acta Geol. Sinica* 86(4), 949–962.
 1062 Song, Z.H., 1986. Review on the study of early Cretaceous angiosperm pollen in China. *Acta*
 1063 *Micropalaeontologica Sinica* 3(4), 373–380 (in Chinese with English abstract).
 1064 Su, N., Zhu, G., Wu, X. D., Yin, H., Lu, Y.C., Zhang, S., 2021. Back-arc tectonic tempos:
 1065 Records from Jurassic–Cretaceous basins in the eastern North China Craton. *Gondwana*
 1066 *Res.* 90, 241–257. <https://doi.org/10.1016/j.gr.2020.12.002>.
 1067 Sullivan, R.F., Boduszynski, M.M., Fetzer, J.C., 1989. Molecular transformations in
 1068 hydrotreating and hydrocracking. *Energ. Fuel.* 3, 603–612.
 1069 <https://doi.org/10.1021/ef00017a013>.
 1070 Sun, G., Zheng, S.L., Sun, X.K., He, C.Q., Pu, T.Y., Shang, Y.K., Zhang, C.B., Yu, Z.Y.,
 1071 Zhao, Y.H., 1992. Recent advance in the research of the strata near the Jurassic-Cretaceous
 1072 boundary in eastern Heilongjiang. *J. Stratigr.* 16(1), 49–54 (in Chinese with English
 1073 abstract).
 1074 Sun, G., Dilcher, D.L., Zheng, S.L., Zhou, Z.K., 1998. In search of the first flower: a Jurassic
 1075 angiosperm, *Archaeofructus*, from Northeast China. *Science* 282, 1692–1695.
 1076 Sun, G., Ji, Q., Dilcher, D.L., Zheng, S.L., Nixon, K., Wang, X.F., 2002. *Archaeofructaceae*, a
 1077 new basal angiosperm family. *Science* 296, 899–904.
 1078 <https://doi.org/10.1126/science.1069439>.
 1079 Sun, W. L. (2006). China coalbed methane basins atlas. Geological Publishing House, Beijing,

1080 pp. 1–233. (in Chinese).

1081 Sun, Y.W., Li, X., G.W., Liu, H., Zhang, Y.L., 2016. Aptian and Albian atmospheric CO₂
 1082 changes during oceanic anoxic events Evidence from fossil *Ginkgo* cuticles in Jilin
 1083 Province, Northeast China. *Cretaceous Res.* 62, 130–141.
 1084 <https://doi.org/10.1016/j.cretres.2015.12.007>.

1085 Tao, M.H., Cui, Z.Q., Chen, G.Q., 2013. Mesozoic spore-pollen assemblages and climate
 1086 fluctuations in northeastern China. *Acta Micropalaeontologica Sinica* 30(3), 275–287 (in
 1087 Chinese with English abstract).

1088 Thompson, K.L., Picard, C.R., Chan, H.M., 2017. Polycyclic aromatic hydrocarbons (PAHs) in
 1089 traditionally harvested bivalves in northern British Columbia, Canada. *Mar. Pollut. Bull.*
 1090 121, 390–399. <https://doi.org/10.1016/j.marpolbul.2017.06.018>.

1091 Trabuco Alexandre, J., van Gilst, R.I., Rodríguez-López, J.P., De Boer, P.L., 2011. The
 1092 sedimentary expression of oceanic anoxic event 1b in the North Atlantic. *Sedimentology*
 1093 58, 1217–1246. <https://doi.org/10.1111/j.1365-3091.2010.01202.x>.

1094 Tsikos, H., Karakitsios, V., van Breugel, Y., Walsworth-Bell, B., Bombardiere, L., Petrizzo,
 1095 M.R., Damst, J.S.S., Schouten, S., Erba, E., Silva, I.P., Farrimond, P., Tyson, R.V.,
 1096 Jenkyns, H.C., 2004. Organic-carbon deposition in the Cretaceous of the Ionian Basin,
 1097 NW Greece: the Paquier Event (OAE 1b) revisited. *Geol. Mag.* 141(4), 401–416.
 1098 <http://dx.doi.org/10.1017/S0016756804009409>.

1099 Wan, X.Q., Li, G., Huang, Q.H., Xi, D.P., Chen, P.J., 2013. Division and correlation of
 1100 terrestrial Cretaceous stages in China. *J. Stratigr.* 37(4), 457–471 (in Chinese with English
 1101 abstract).

1102 Wang, W.F., Lu, S.K., Guo, Y.X., Sun, Y.P., 1998. Tectonic geometry and type of traps in
 1103 Fuxin Basin. *J. Univ. Petrol. China* 22(3), 29–33 (in Chinese with English abstract).

1104 Wang, D.D., Yin, L.S., Shao, L.Y., Lv, D.W., Liu, H.Y., Wang, S., Dong, G.Q., 2021a.
 1105 Characteristics and evolution of inertinite abundance and atmospheric *p*O₂ during China's
 1106 coal-forming periods. *J. Palaeogeogr.* 10, 13. [https://doi.org/10.1186/s42501-021-00090-](https://doi.org/10.1186/s42501-021-00090-4)
 1107 4.

1108 Wang, D.D., Mao, Q., Dong, G.Q., Yang, S.P., Lv, D.W., Yin, L.S., 2019a. The Primary
 1109 investigation of the genetic mechanism of inertinite in the Middle Jurassic inertinite-rich

1110 coal seams of the southern Ordos Basin. *J. Geol. Res.* 1(3), 1–15.

1111 Wang, S., Shao, L.Y., Yan, Z.M., Shi, M.J., Zhang, Y.H., 2019b. Characteristics of Early
 1112 Cretaceous wildfires in peat-forming environment, NE China. *J. Palaeogeogr.* 103(7),
 1113 1653–1690. <https://doi.org/10.1186/s42501-019-0035-5>.

1114 Wang, S., Shao, L.Y., Li, J.X., Li, J.A., Jones, T., Zhu, M.Y., Zhou, J.M., 2021b. Coal
 1115 petrology of the Yimin Formation (Albian) in the Hailar Basin, NE China:
 1116 Paleoenvironments and wildfires during peat formation. *Cretaceous Res.* 124, 104815.
 1117 <https://doi.org/10.1016/j.cretres.2021.104815>.

1118 Wildman, R.A., Hickey, L.J., Dickinson, M.B., Berner, R.A., Robinson, J.M., Dietrich, M.,
 1119 Essenhight, R.H., Wildman, C.B., 2004. Burning of forest materials under late Paleozoic
 1120 high atmospheric oxygen levels. *Geology*, 32(5), 457–460.
 1121 <https://doi.org/10.1130/G20255.1>.

1122 Wu, F.Y., Xu, Y.G., Zhu, R.X., Zhang, G.W., 2014. Thinning and destruction of the cratonic
 1123 lithosphere: a global perspective. *Sci. China Earth Sci.* 57 (2), 2878–2890.

1124 Xi, D.P., Wan, X.Q., Li, G.B., Li, G., 2019. Cretaceous integrative stratigraphy and timescale
 1125 of China. *Sci. China Earth Sci.* 62(1), 256–286. [https://doi.org/10.1007/s11430-017-9262-](https://doi.org/10.1007/s11430-017-9262-y)
 1126 [y](https://doi.org/10.1007/s11430-017-9262-y).

1127 Xu, D.B., Li, B.F., Chang, Z.L., Zhang, J.B., Cai, H.A., 2012. Study of U–Pb isotopic age and
 1128 sequence of the Cretaceous volcanic rocks and coal-searching in Fuxian–Zhangwu–
 1129 Heishan area, western Liaoning Province. *Earth Sci. Front.* 19 (6), 155–166 (in Chinese
 1130 with English abstract).

1131 Xu, X.T., Shao, L.Y., 2018. Limiting factors in utilization of chemical index of alteration of
 1132 mudstones to quantify the degree of weathering in provenance. *J. Palaeogeogr.* 20(3), 515–
 1133 522. (in Chinese with English abstract).

1134 Xu, X.T., Shao, L.Y., Lan, B., Wang, S., Hilton, J., Qin, J., Hou, H., Zhao, J., 2020a.
 1135 Continental chemical weathering during the Early Cretaceous Oceanic Anoxic Event (OAE
 1136 1b): a case study from the Fuxin fluvio-lacustrine basin, Liaoning Province, NE China. *J.*
 1137 *Palaeogeogr.* 9(2), 246–266. <https://doi.org/10.1186/s42501-020-00056-y>.

1138 Xu, X.T., Shao, L.Y., Fu, Y.F., Wang, D.D., Cai, H.A., Qin, J.Y., Hou, H.H., Zhao, J., 2020b.
 1139 Sequence palaeogeography, lacustrine basin evolution, and coal accumulation in the Lower

1140 Cretaceous Fuxin continental faulted basin, China. *Geol. J.* 55(2), 1195–1215.
 1141 <https://doi.org/10.1002/gj.3483>.

1142 Xu, X.T., Shao, L.Y., Eriksson, K.A., Pang, B., Wang, S., Yang, C.X., Hou, H.H., 2022.
 1143 Terrestrial records of the early Albian Ocean Anoxic Event: Evidence from the Fuxin
 1144 lacustrine basin, NE China. *Geosci. Front.* 13(1), 101275.
 1145 <https://doi.org/10.1016/j.gsf.2021.101275>.

1146 Xu, Y., Uhl, D., Zhang, N., Zhao, C., Qin, S., Liang, H., Sun, Y., 2020c. Evidence of
 1147 widespread wildfires in coal seams from the Middle Jurassic of Northwest China and its
 1148 impact on paleoclimate. *Palaeogeogr. Palaeoclimatol. Palaeoecol.* 559, 109819.
 1149 <https://doi.org/10.1016/j.palaeo.2020.109819>.

1150 Yan, Z.M., Shao, L.Y., Glasspool, I.J., Wang, J., Wang, X.T., Wang, H., 2019. Frequent and
 1151 intense fires in the final coals of the Paleozoic indicate elevated atmospheric oxygen
 1152 levels at the onset of the End-Permian Mass Extinction Event. *Int. J. Coal Geol.* 207, 75–
 1153 83. <https://doi.org/10.1016/j.coal.2019.03.016>.

1154 Yang, Y.K., 1996. Atlas for Coal Petrography of China. China University of Mining and
 1155 Technology Press, Xuzhou, pp. 1–99. (in Chinese).

1156 Zakir Hossain, H.M., Sampei, Y., Roser, B.P., 2013. Polycyclic aromatic hydrocarbons (PAHs)
 1157 in late Eocene to early Pleistocene mudstones of the Sylhet succession, NE Bengal Basin,
 1158 Bangladesh: Implications for source and paleoclimate conditions during Himalayan uplift.
 1159 *Org. Geochem.* 56, 25–39. <https://doi.org/10.1016/j.orggeochem.2012.12.001>.

1160 Zhang, J., 2003. Geothermal resources hosting condition analysis, Dongliang District, Fuxin
 1161 Basin. *Coal Geol. China* 15(6), 37–39. (in Chinese with English abstract).

1162 Zhang, Q., Zhang, M.S., Li, X.B., Wang, Y.N., Liu, X.S., Zhang, M.M., 2016. Stratigraphic
 1163 sequences and zircon U–Pb dating of Yixian Formation in Caozhuang area of Xingcheng,
 1164 western Liaoning. *Global Geol.* 35(1), 51–65. (in Chinese with English abstract).

1165 Zhang, Z.H., Wang, C.S., Lv, D.W., Hayd, W.W., Wang, T.T., Cao, S., 2020. Precession-scale
 1166 climate forcing of peatland wildfires during the early middle Jurassic greenhouse period.
 1167 *Glob. Planet. Chang.* 184, 103051. <https://doi.org/10.1016/j.gloplacha.2019.103051>.

1168 Zhao, X.D., Zheng, D.R., Wang, H., Fang, Y.N., Xue, N.H., Zhang, H.C., 2022. Carbon cycle
 1169 perturbation and mercury anomalies in terrestrial Oceanic Anoxic Event 1b from Jiuquan

- Basin, NW China. Geological Society, London, Special Publications 521.
- Zhou, W.F., Algeo, T.J., Luo, G.M., Ruan, X.Y., Chen, Z.Q., Xie, S.C., 2021. Hydrocarbon compound evidence in marine successions of South China for frequent wildfires during the Permian-Triassic transition. *Glob. Planet. Chang.* 200, 103472. <https://doi.org/10.1016/j.gloplacha.2021.103472>.
- Zhou, Z.H., Barrett, P.M., Hilton, J., 2003. An exceptionally preserved Lower Cretaceous ecosystem. *Nature* 421, 807–814. <https://doi.org/10.1038/nature01420>.
- Zhu, R.X., Lo, C.H., Shi, R.P., Shi, G.G., Pan, Y.X., Sha, J., 2004. Palaeointensities determined from the middle Cretaceous basalt in Liaoning Province, northeastern China. *Phys. Earth Planet. In.* 142, 49–59. <https://doi.org/10.1016/j.pepi.2003.12.013>.
- Zhu, R.X., Zhang, H.F., Zhu, G., Meng, Q.R., Fan, H.R., Yang, J.H., Wu, F.Y., Zhang, Z.Y., Zheng, T.Y., 2017. Craton destruction and related resources. *Int. J. Earth Sci.* 106, 2233–2257.
- Zhu, Z.M., Yan, J.F., Shen, B., Zhou, J.Y., 2007. Co-existing formation of multi-energy resources in the Fuxin Basin analysis from tectonic-thermal events. *Adv. Earth Sci.* 22(5), 468–479. (in Chinese with English abstract).

Figures and table captions

Fig. 1. Location of the Fuxin Basin. a. Outline map of China showing position of Fuxin Basin. b. Enlargement of the top right part of Figure 1a showing position of the Fuxin basin and tectonic features (modified after Zhu et al., 2007). c. Global palaeogeographic map of the early Cretaceous showing approximate location of study area (modified from the ~110 Ma map of the webpage <https://deeptimemaps.com/global-paleogeography-and-tectonics-in-deep-time>). Abbreviations: AfP = African Plate; AnP = Antarctic Plate; Arp = Arabian Plate; AuP = Australian Plate; CAP = Central Asian Plate; EP = European Plate; IP = Indian Plate; NAP = North America Plate; NCP = North China Plate; SAmP = South American Plate; SAsP = Southeast Asian Plate; SCP = South China Plate; SP = Siberian Plate.

Fig. 2. Geology and stratigraphy of the Fuxin Basin. a. Geologic map of the Fuxin Basin (modified after Sun, 2006); cross-section A-A' is modified from the interpreted seismic profile

(Zhu et al., 2007; Su et al., 2021). b. Stratigraphic succession for the western Liaoning region during the Aptian–Albian interval with flora assemblages (Deng et al., 2012) and isotopic ages. Age sources: ① from Zhang et al. 2016; ② from Xu et al. 2012; ③ from Su et al. 2021; ④ from He et al. 2004; ⑤ from Xu et al. 2021; ⑥ from Zhu et al. 2004. I, II, III and IV represent the first, second, third and fourth members of the Shahai Formation, respectively. Abbreviations: Flora assem. = Flora assemblages.

Fig. 3. Stratigraphic distribution of kerogen macerals from mudstone samples in borehole DY-1 from the Lower Cretaceous Shahai and Fuxin formations in the Fuxin Basin. The interpretation of the sedimentary environments and zircon U-Pb age is from Xu et al. (2022). Abbreviations: J. F. = Jiufotang Formation; S. F. = Sunjiawan Formation; Sed. en. = Sedimentary environments.

Fig. 4. Photomicrographs showing microstructural characteristics of kerogen macerals from borehole DY-1 in the early Cretaceous Fuxin Basin. a and b, sapropelinite (transmitted light, 600m and 1095.5m). c and d, vitrinite (transmitted light, 714.5m). e and f, conifer pollen (transmitted light and fluorescence, respectively, 714.5m). g. fern spore (transmitted light, 714.5m). h. conifer pollen (transmitted light, 413m). i. conifer pollen (transmitted light, 714.5m). j. conifer pollen (transmitted light, 856m). k, l and m, inertinite (transmitted light, 413m, 1146m and 946.3m).

Fig. 5. Photographs of macroscopic charcoal and plant fossils from borehole DY-1 and outcrops in the early Cretaceous Fuxin Basin. a. Small charcoal fragments with black color in sandstone, 541m. b. Charcoalified wood fragments in mudstone, 625.8m. c. Small charcoals showing long strips in fine sandstone, 847.5m. d-f. Lacustrine mudstone with abundant charred plant fossil fragments, the depth is 862.2m, 919.8m and 920.5m respectively. g. Small charcoalified wood fragments in lacustrine mudstone, 1093.8m. h. Charred tree trunk fossil in lacustrine mudstone, 1135.9m. i. Charcoalified tree trunk fossil and angular wood fragments Haizhou open-pit coal mine section; the hammer is 30 cm long. j. Abundant charcoal fragments in sandstones showing cubic blocks of charcoalified wood, Haizhou open-pit coal mine section; the hammer is 30 cm long. k. Grey mudstone with cycad fossil fragments, 540m. l.

1231 Grey siltstone with cycad fossil fragments, Haizhou open-pit coal mine section.

1232

1233 Fig. 6. Photomicrographs of inertinite contents in mudstone from borehole DY-1 in the early
1234 Cretaceous Fuxin Basin. a. Inertinite with compressed and broken cell walls, reflected light,
1235 413m. b and c, inertinite, reflected light, 459m and 800m. d. Inertinite with regular and
1236 complete arrangement of cellular structure with relatively high reflectance, 1095.5m.

1237

1238 Fig. 7. Scanning electron micrographs of inertinite in mudstone from borehole DY-1; early
1239 Cretaceous Fuxin Basin. a. Detail of tracheids with uniseriate, contiguous, circular pits in
1240 walls, 458.6m. b. Longitudinal section of tracheids showing homogenized cell walls, 625.8m.
1241 c. Transverse section of vessels with high density, 847.5m. d. Longitudinal section of tracheids
1242 with tracheids broken by compaction, 868.9m. e. Cross-section with homogenized cell walls,
1243 919.8m. f. Cross-section showing relatively well-preserved tracheids with cellular structure,
1244 1093.8m.

1245

1246 Fig. 8. Total ion current traces of aromatic hydrocarbon fractions for the ten mudstone samples
1247 in borehole DY-1 from the early Cretaceous Fuxin Basin. Structures for selected PAHs show
1248 the total ion current chromatograms of samples DY-1-5, DY-1-8 and DY-1-16. IS-internal
1249 standard; VI-Phenanthrene; VII-Anthracene; VIII-Retene; IX-Fluoranthene; X-
1250 Benzo[a]fluorine; XI-Benzo[b]fluorine; XII-Pyrene; XIII-Benz(a)anthracene; XIV- Chrysene;
1251 XV-Benzofluoranthenes; XVI-Benzo(e)pyrene; XVII-Benzo(a)pyrene; XVIII-Perylene.

1252

1253 Fig. 9. Carbon isotopic correlation of the OAE1b event between marine and terrestrial
1254 successions. Carbon isotopic data collected from the borehole DY-1 in the Fuxin Basin, NE
1255 China. Data collated for the Fuxin terrestrial basin from Xu et al. (2022), the Chong'an
1256 terrestrial section in SE China from Hu et al. (2014), the Hanxiagou terrestrial section in NW
1257 China from Zhao et al. (2022), the marine Vocontian Basin (SE France) from Herrle et al.
1258 (2004), the marine Poggio le Guaine Section from Matsumoto et al. (2020), the marine Andean
1259 Basin, northern Peru from Navarro-Ramirez et al. (2015) and ODP site 1049 off northern
1260 Florida on the Blake Nose escarpment from Huber et al. (2011).

1261

1262 Fig. 10. Correlation of kerogen macerals, wildfire types, organic carbon isotopes ($\delta^{13}\text{C}_{\text{org}}$) and
1263 total organic carbon (TOC) across the early Albian OAE 1b. Depth locations are shown in Fig.
1264 4. The zircon U-Pb age, organic carbon isotopes ($\delta^{13}\text{C}_{\text{org}}$) and total organic carbon (TOC) is
1265 from Xu et al. (2022). Abbreviations: J. F. = Jiufotang Formation; S. F. = Sunjiawan Formation.
1266

1267 Fig. 11. Predictions of $p\text{O}_2$ in Unit C during the early Albian in the Fuxin Basin based on the
1268 model proposed by Glasspool et al. (2015). S-shaped curves are assumed to ensure a smooth
1269 transition from 0% inertinite at low oxygen levels to 100% inertinite at high oxygen levels.
1270 However, the curve above 35% $p\text{O}_2$ is relatively unimportant as plant biomass can still burn so
1271 readily as to be incompatible with sustained plant growth (Jones and Chaloner, 1991). The two
1272 blue curves represent the error interval. Red curve represents the best estimate for $p\text{O}_2$ level.
1273 Abbreviations: Min. = minimum; Max. = maximum; Aver. = average.

1274

1275 Fig. 12. Schematic model illustrating possible relationship between wildfire activity and anoxia
1276 in the Fuxin lacustrine basin during the early Albian OAE 1b. Wildfires and associated post-
1277 fire erosion intensified the transport rate of nutrients and organic matter from continents into
1278 lakes under conditions of intensified continental chemical weathering, thereby contributing to
1279 eutrophication and anoxia in lacustrine and contemporaneous oceanic systems.

1280

1281 Table 1 Kerogen macerals and inertinite reflectance values of mudstone samples from the
1282 Lower Cretaceous Shahai and Fuxin formations in the Fuxin Basin.

1283

1284 Table 2 Concentration of the PAHs of ten mudstones from the early Cretaceous Fuxin Basin.

1285

Fig. 1

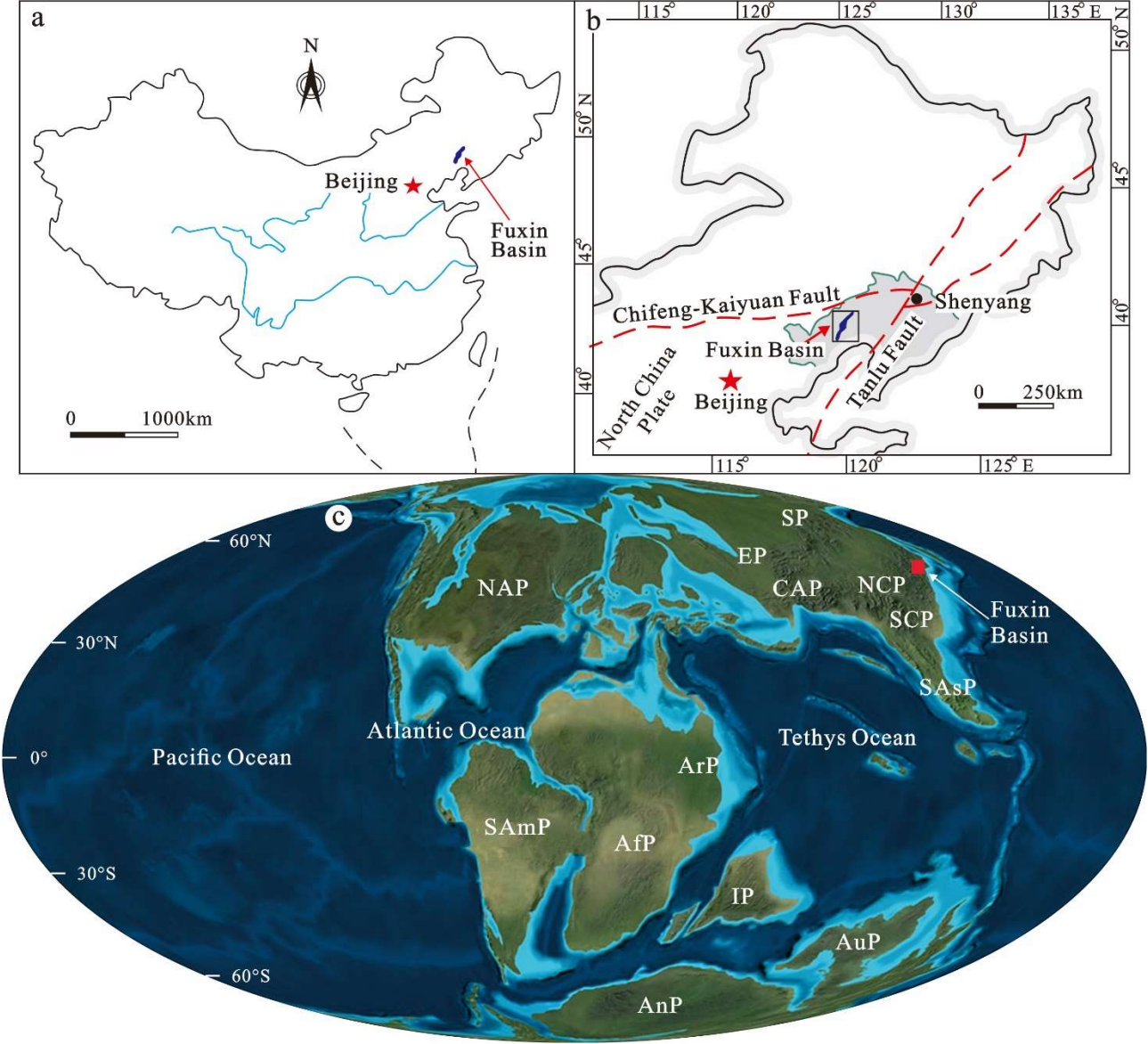


Fig. 2

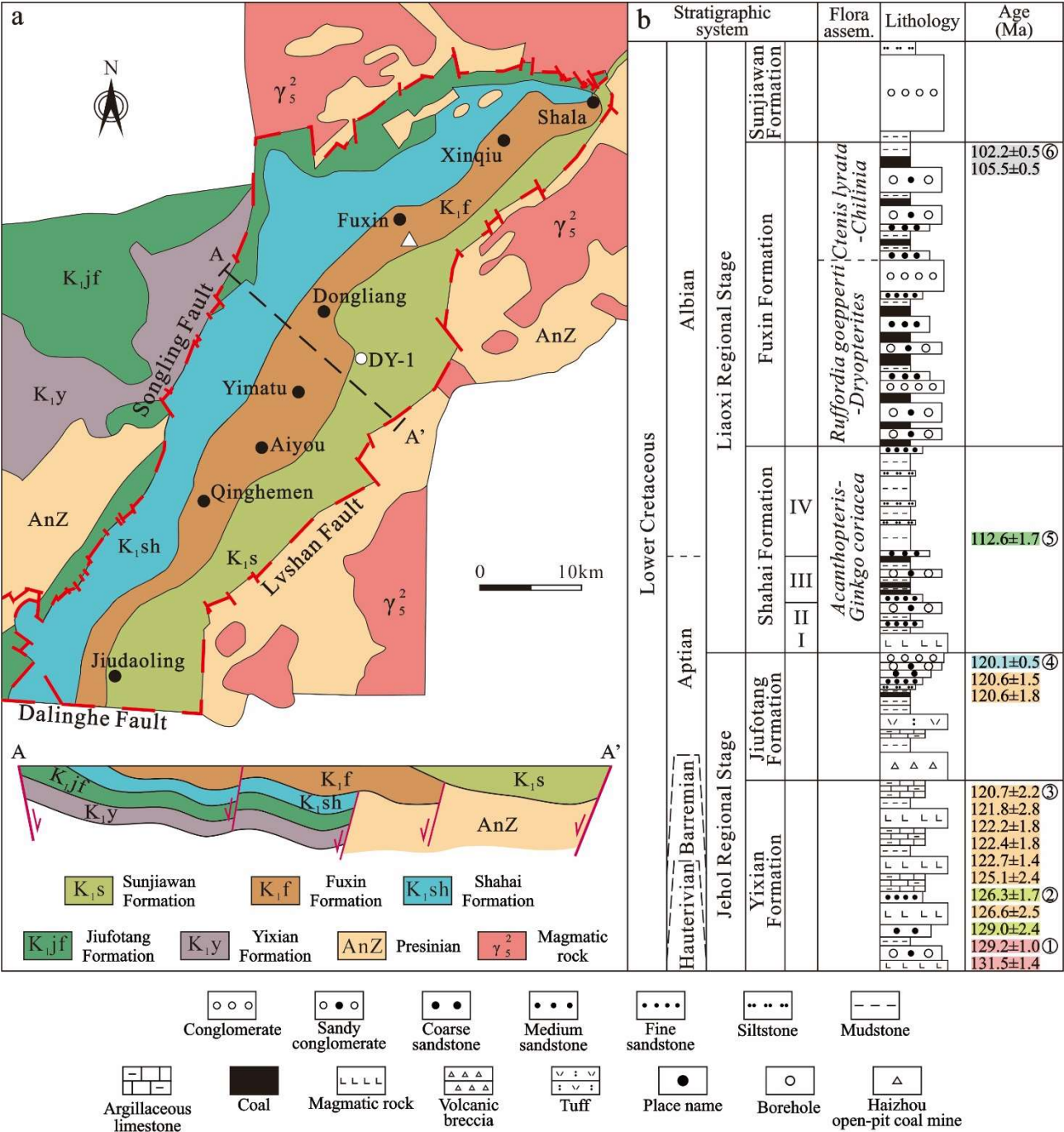


Fig. 3

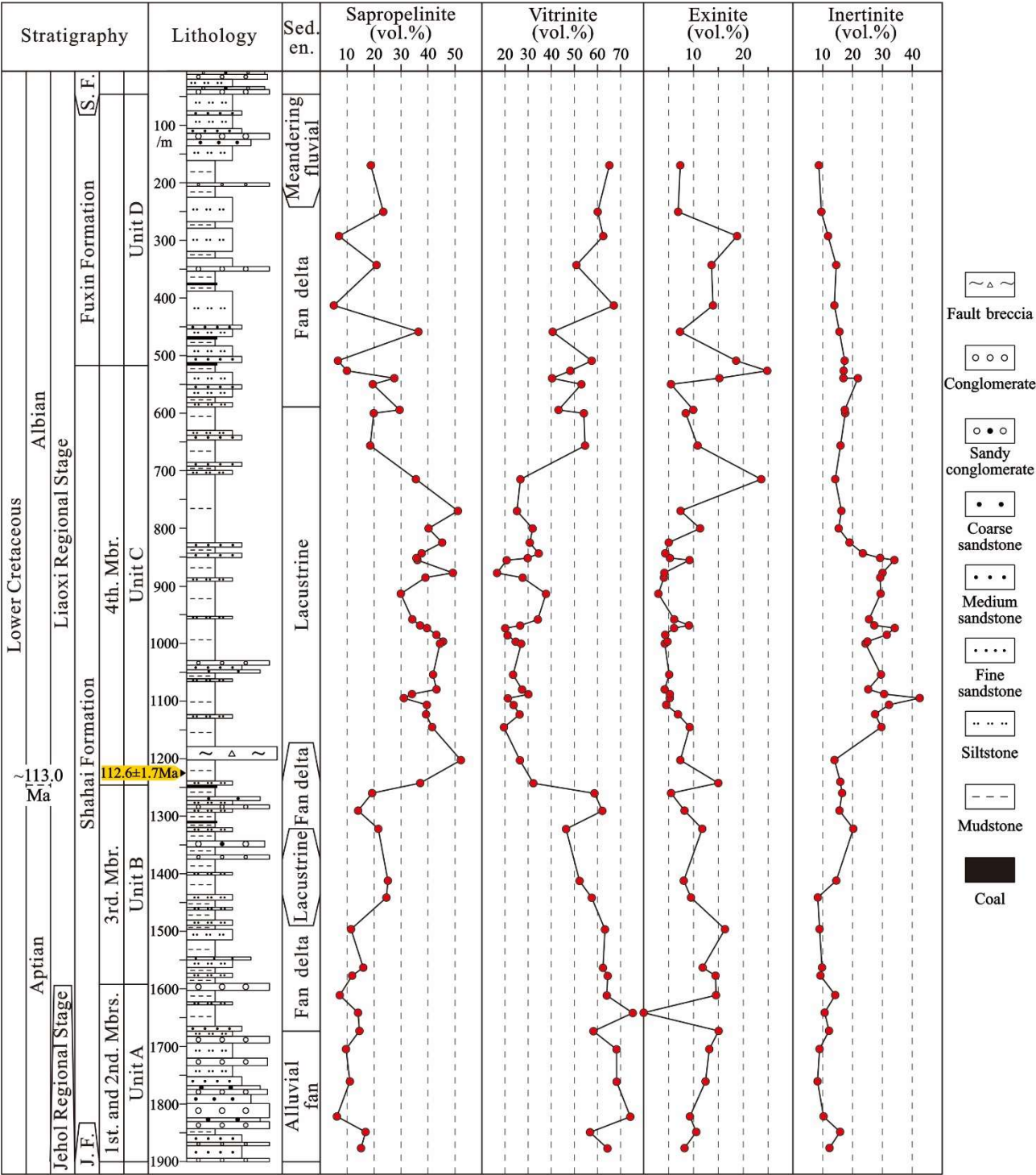


Fig. 4

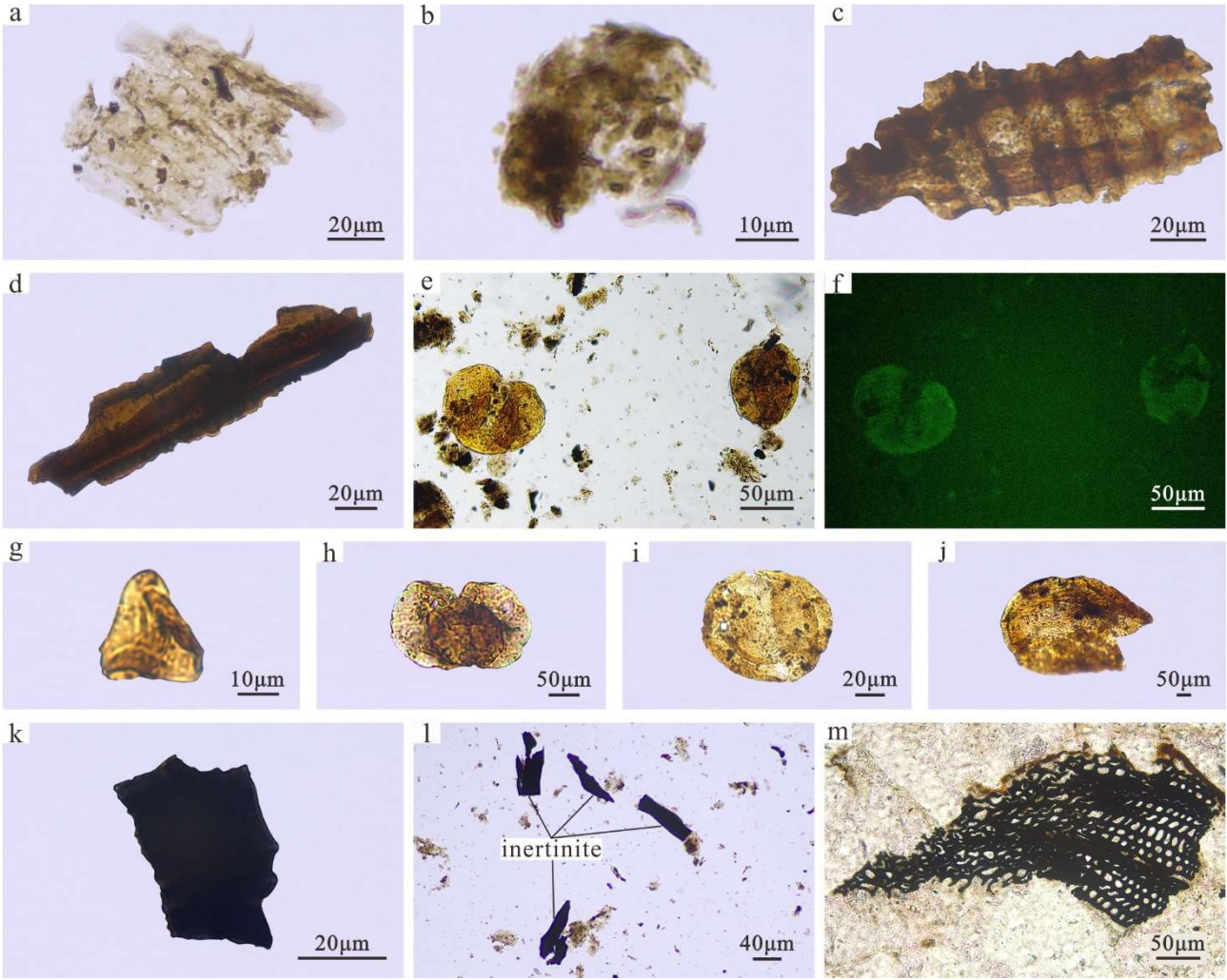


Fig. 5

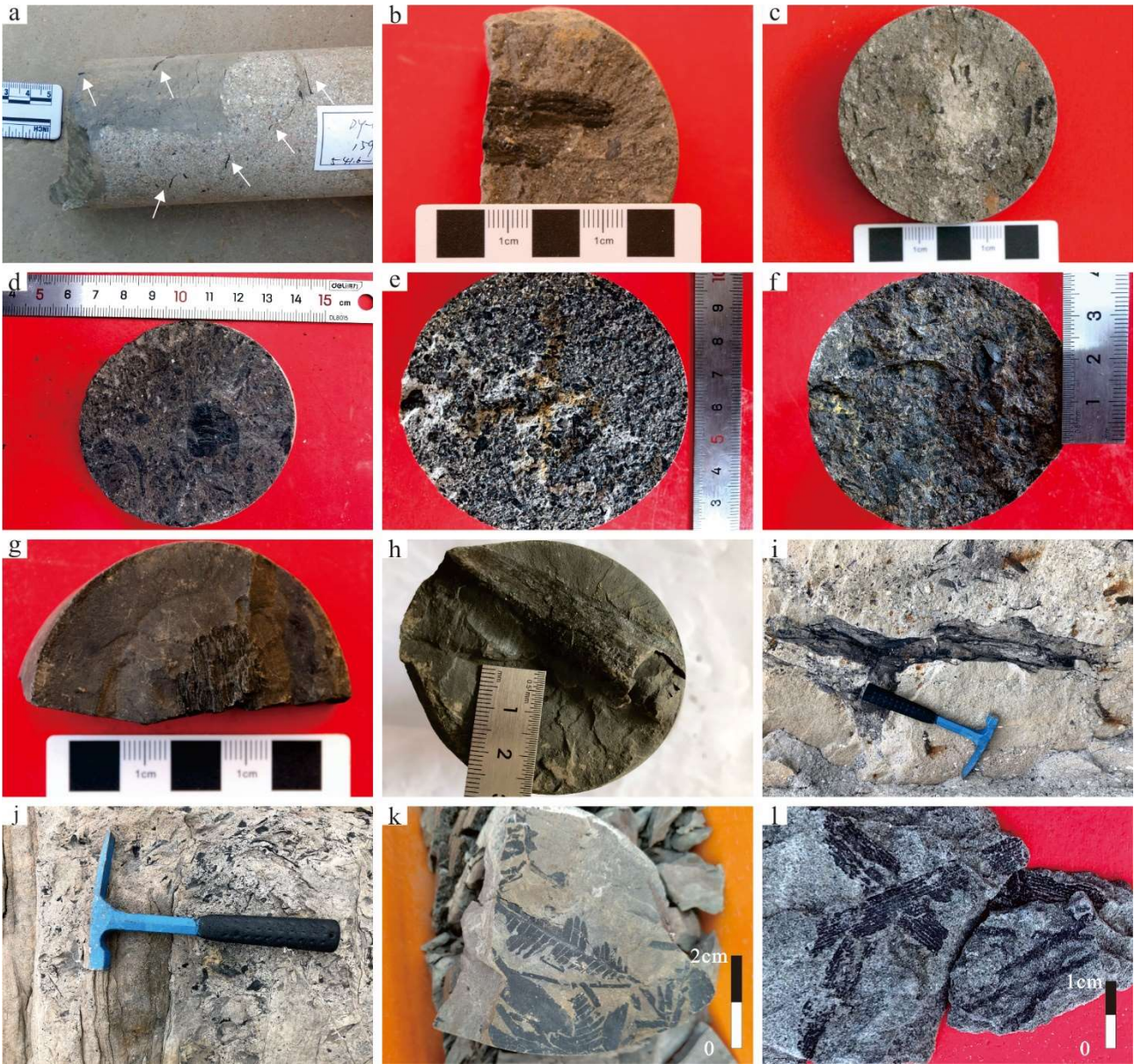


Fig. 6

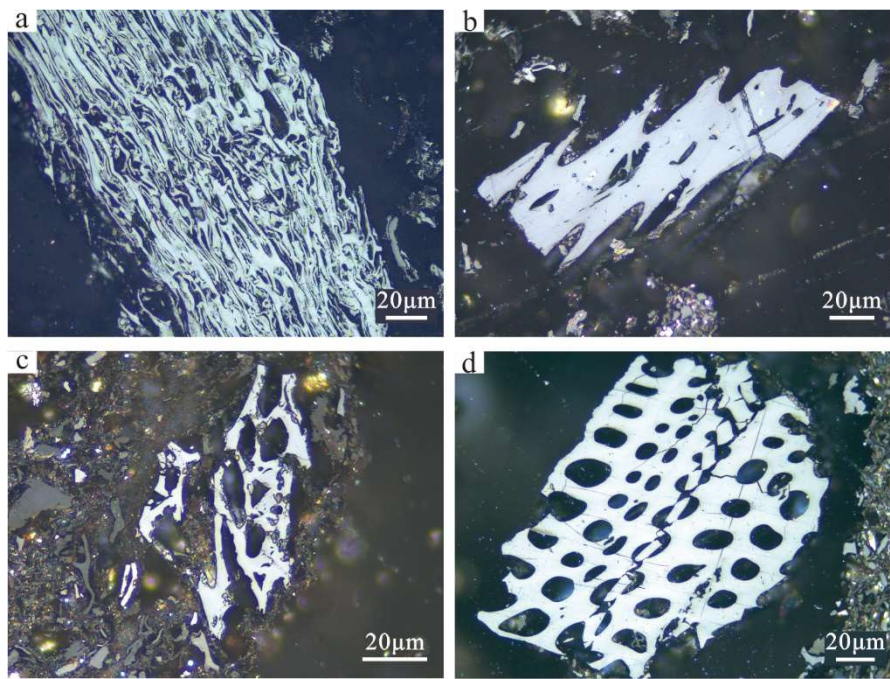


Fig. 7

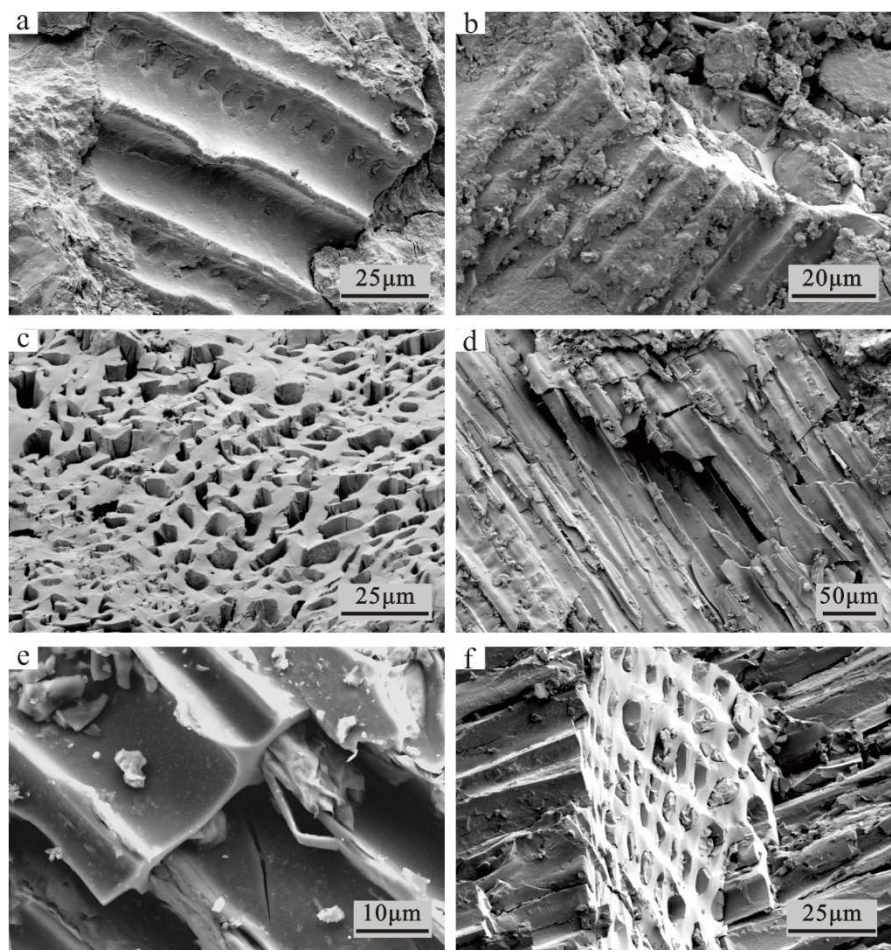


Fig. 8

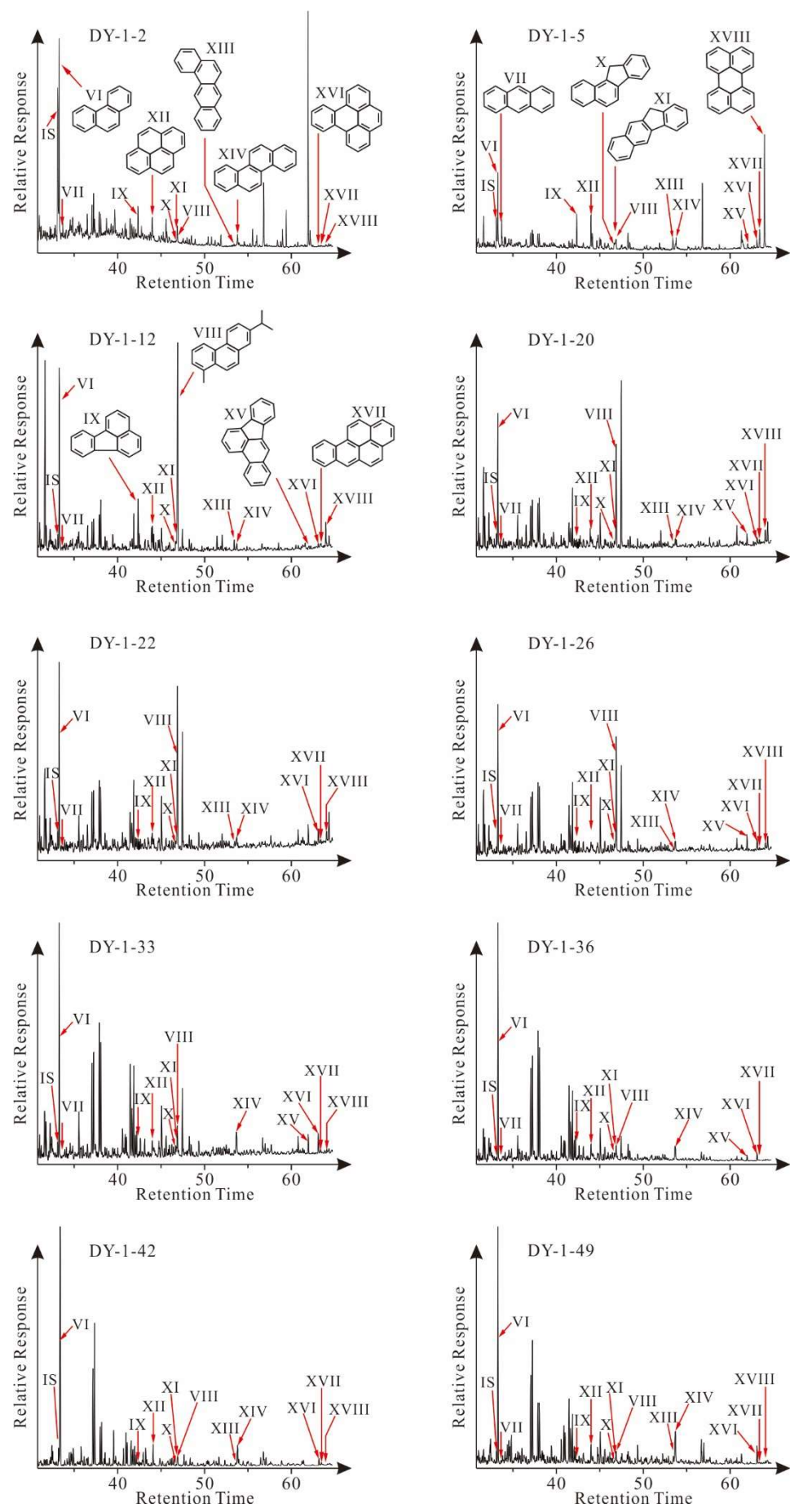


Fig. 9

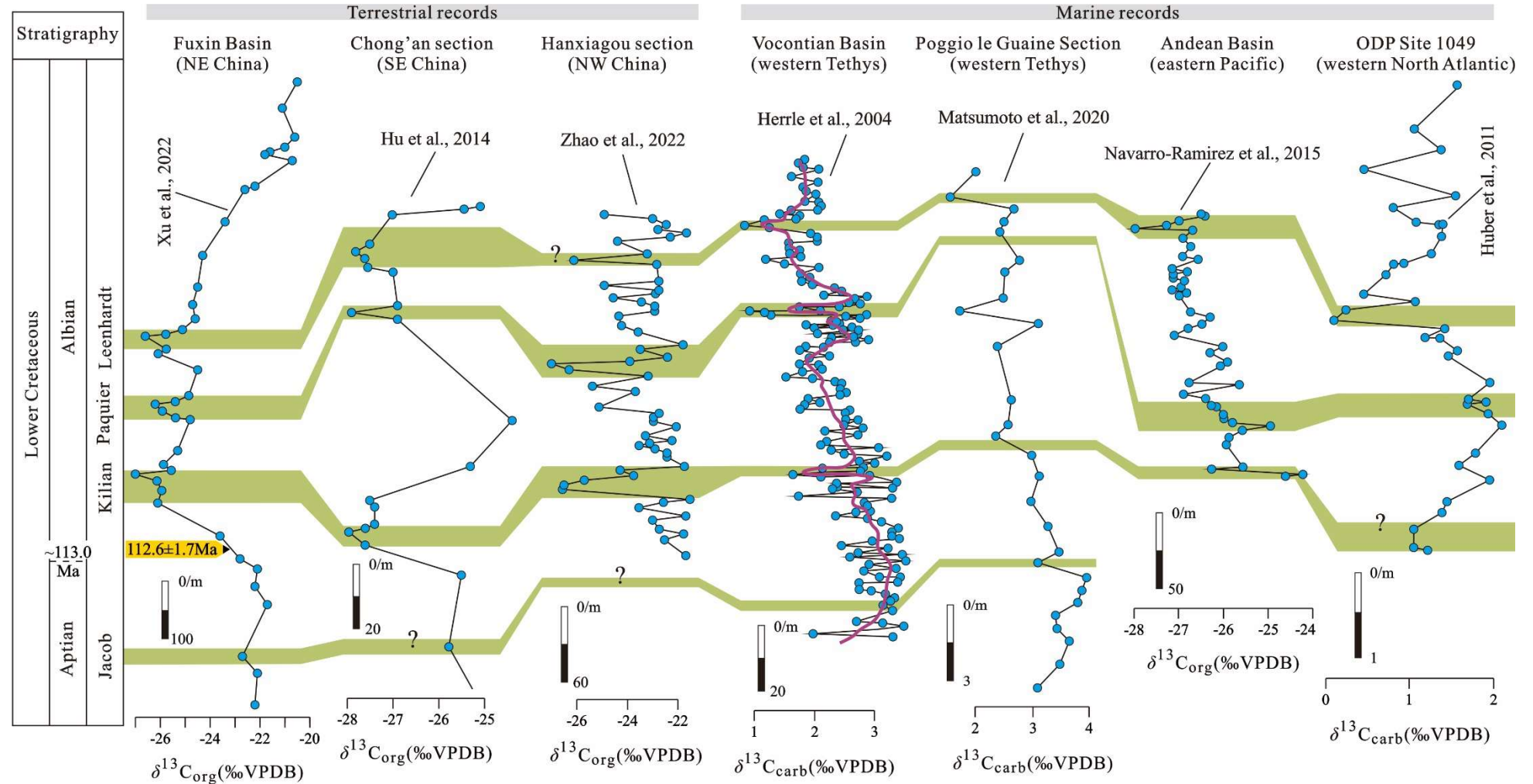


Fig. 10

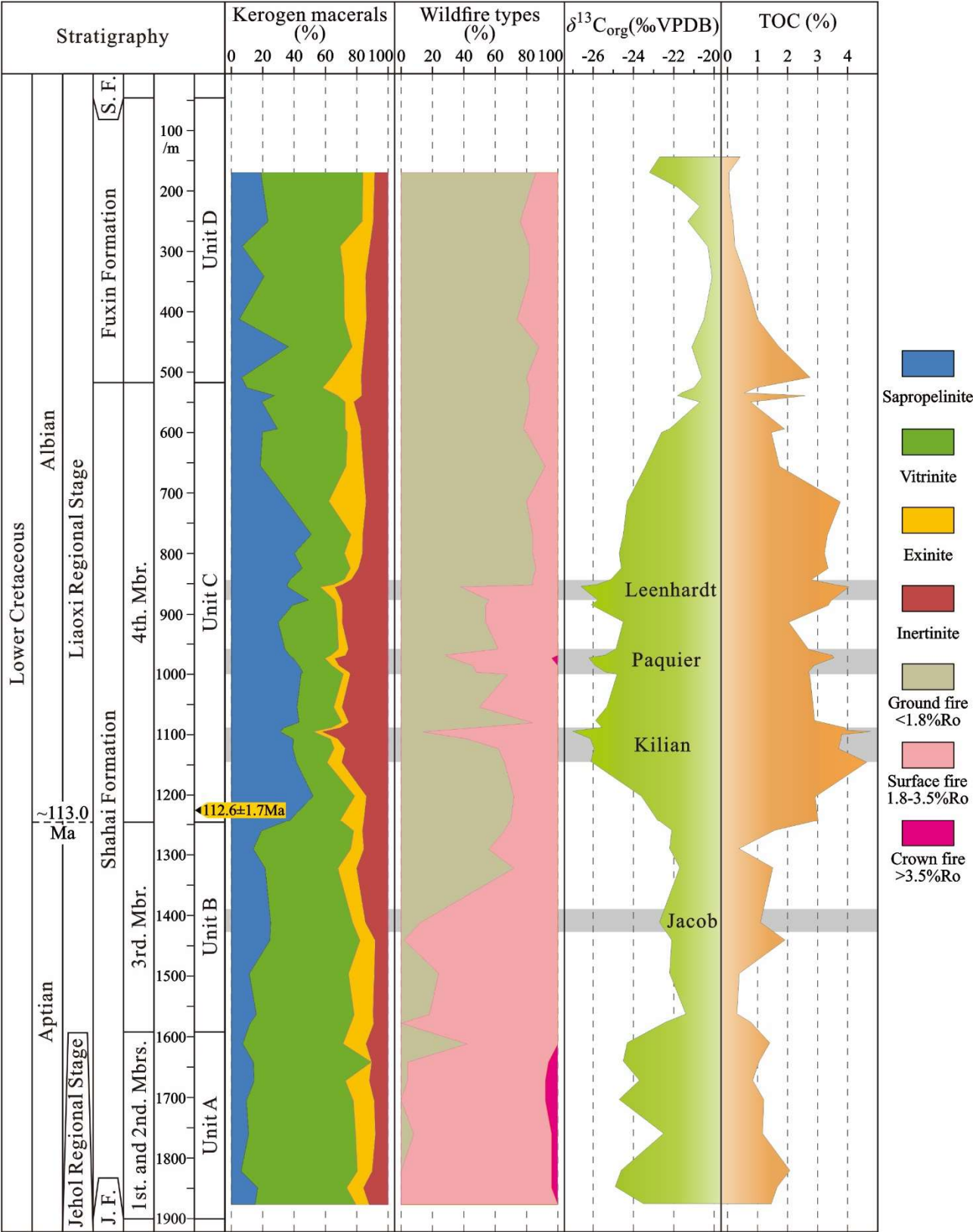


Fig. 11

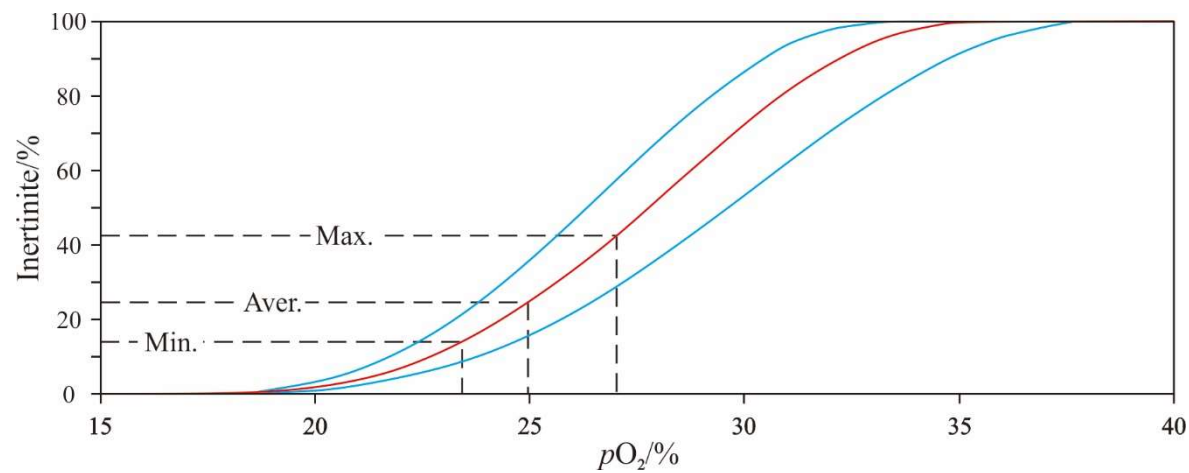


Fig. 12

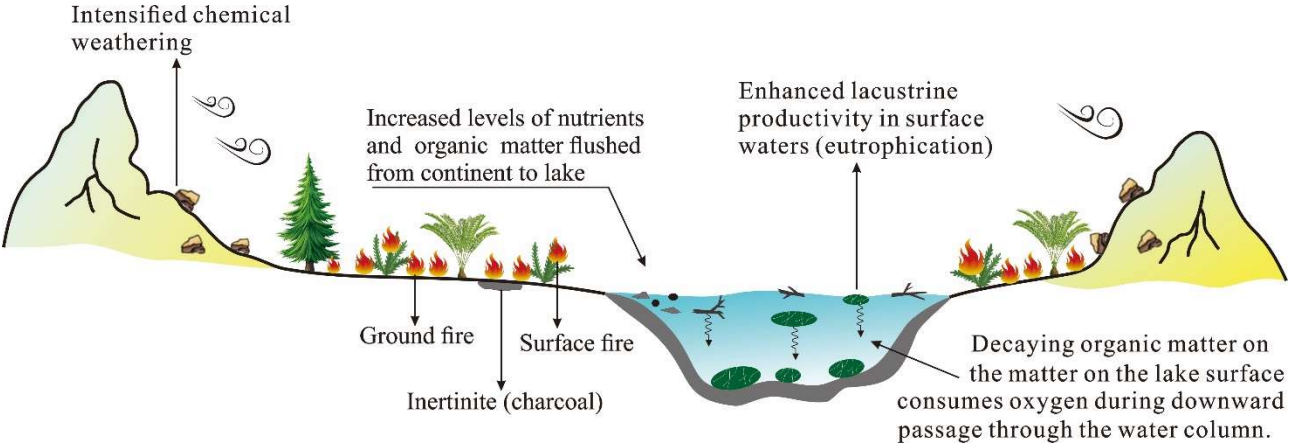


Table 1

Organic carbon isotope ($\delta^{13}\text{C}_{\text{org}}$), total organic carbon (TOC), kerogen macerals and inertinite reflectance values of mudstone samples from the Lower Cretaceous Shahai and Fuxin formations in the Fuxin Basin.

Borehole	Sample	Depth/m	$\delta^{13}\text{C}_{\text{org}}$	TOC	Kerogen macerals (vol.%, mmf)				Inertinite reflectance (%Ro)		
			‰VPD	%	Sap.	Vitr.	Exi.	Iner.	Min.	Max.	Aver.
	DY-1-1	144	-22.7	0.42	-	-	-	-	-	-	-
	DY-1-2	170	-23.2	0.05	18.8	65.1	7.3	8.7	0.9	2.4	1.4
	DY-1-3	194.6	-21.8	0.05	-	-	-	-	-	-	-
	DY-1-4	225.5	-20.7	0.12	-	-	-	-	-	-	-
	DY-1-5	251	-21.3	0.19	23.4	60.1	6.9	9.6	1.2	2.1	1.7
	DY-1-6	292.6	-20.3	0.25	6.9	62.5	18.8	11.8	0.8	2.2	1.4
	DY-1-7	342.7	-20.1	0.61	20.9	50.9	13.6	14.5	0.9	2.2	1.4
	DY-1-8	413	-20.5	1.01	5.1	67.1	13.9	13.9	1.0	2.5	1.6
	DY-1-9	459	-21.1	1.72	36.5	40.6	7.3	15.6	1.1	2.3	1.6
	DY-1-10	509.5	-20.6	2.75	6.6	57.5	18.6	17.4	0.9	2.6	1.6
	DY-1-11	527	-21.0	0.93	9.9	48.2	24.8	17.0	1.1	2.1	1.6
	DY-1-12	535	-21.6	0.57	-	-	-	-	-	-	-
	DY-1-13	540	-21.8	2.59	27.5	40.4	15.2	17.0	0.6	2.0	1.3
	DY-1-14	549.5	-20.7	0.77	19.5	53.0	5.5	22.0	0.9	2.0	1.4
	DY-1-15	594.5	-22.2	1.90	29.5	43.2	10.0	17.4	0.8	2.4	1.5
	DY-1-16	600	-22.6	1.46	19.9	54.1	8.4	17.5	0.8	2.1	1.4
	DY-1-17	656	-23.4	1.73	18.6	54.6	10.8	16.0	1.0	2.0	1.4
	DY-1-18	714.5	-24.3	3.76	35.5	26.6	23.6	14.2	0.8	2.1	1.4
	DY-1-19	769.5	-24.5	3.33	51.1	25.2	7.4	16.3	0.8	2.3	1.6
	DY-1-20	800	-24.7	3.23	40.2	32.0	11.3	16.5	1.1	2.3	1.5
	DY-1-21	824.9	-24.6	3.34	45.3	30.7	5.0	19.0	1.1	2.4	1.5
	DY-1-22	843.3	-25.1	2.79	37.7	34.6	4.3	23.5	0.9	2.2	1.5
	DY-1-23	852.2	-25.8	3.65	35.7	29.8	5.3	29.2	1.2	2.7	1.6
	DY-1-24	856	-26.6	4.05	36.1	20.7	9.2	34.0	1.5	2.9	1.9
	DY-1-25	877.7	-25.7	3.45	49.2	16.6	4.1	30.1	1.4	2.5	1.8
	DY-1-26	886	-26.1	3.36	39.0	27.6	4.1	29.3	1.2	2.8	1.8
	DY-1-27	914.5	-24.5	2.04	29.9	37.7	2.9	29.4	1.1	2.4	1.8
	DY-1-28	958.5	-24.9	2.70	34.2	34.2	6.1	25.5	1.2	2.9	1.8
	DY-1-29	968.6	-25.4	3.49	37.1	26.6	9.1	27.3	1.0	2.9	2.1
	DY-1-30	974	-26.2	3.55	39.6	20.1	6.1	34.1	1.2	3.8	2.3
	DY-1-31	985.9	-25.9	2.89	43.1	21.1	4.3	31.5	1.2	2.8	1.9
	DY-1-32	997	-25.4	2.69	45.6	24.6	4.8	25.0	1.3	2.9	1.8
	DY-1-33	1000	-24.8	2.74	44.4	27.0	4.2	24.3	0.9	2.5	1.8
	DY-1-34	1055	-25.3	2.86	41.9	23.5	5.1	29.5	0.9	2.6	1.8
	DY-1-35	1080.4	-25.9	2.90	43.2	27.4	4.2	25.3	1.3	2.4	1.7
	DY-1-36	1088.3	-25.6	3.92	34.1	30.1	5.2	30.6	1.0	3.0	1.8
	DY-1-37	1095.5	-27.0	4.76	31.0	21.2	5.2	42.5	1.7	3.3	2.3
	DY-1-38	1107.5	-26.1	3.78	39.5	23.7	4.5	32.2	1.4	3.0	2.1
	DY-1-39	1123.3	-25.9	3.70	39.3	26.3	6.9	27.5	1.3	2.6	1.8

DY-1-40	1146	-26.1	4.64	41.5	19.6	9.2	29.7	1.1	3.0	1.8
DY-1-41	1202.5	-23.6	2.92	52.2	26.5	7.4	14.0	1.3	2.3	1.7
DY-1-42	1242.3	-22.8	3.02	37.1	32.2	15.0	15.6	1.3	2.3	1.7
DY-1-43	1260.4	-22.1	1.58	19.3	58.7	5.5	16.5	1.1	2.8	1.8
DY-1-44	1291.2	-22.2	0.38	14.1	62.1	8.2	15.6	0.8	2.6	1.8
DY-1-45	1322.3	-21.7	1.51	21.6	46.4	11.8	20.3	0.8	2.6	1.6
DY-1-46	1412.5	-22.7	1.10	25.1	52.3	8.0	14.6	1.6	3.4	2.2
DY-1-47	1441.2	-22.1	1.92	24.6	57.5	9.5	8.4	1.8	3.4	2.6
DY-1-48	1496.3	-22.2	0.40	11.4	63.3	16.3	9.0	0.8	3.3	2.0
DY-1-49	1563.8	-21.4	0.32	16.0	62.4	11.9	9.8	1.0	3.3	2.2
DY-1-50	1578	-22.4	0.78	11.9	64.4	14.4	9.3	1.8	3.1	2.4
DY-1-51	1612	-24.3	1.41	7.3	64.0	14.5	14.2	1.0	3.0	1.9
DY-1-52	1642	-24.5	1.06	14.0	75.3	0.0	10.7	1.6	4.3	2.6
DY-1-53	1673.3	-23.7	0.84	14.6	58.3	15.0	12.1	1.8	3.8	2.6
DY-1-54	1705.3	-24.7	1.21	9.6	68.3	13.2	9.0	2.0	3.7	2.8
DY-1-55	1761	-22.5	1.17	11.0	68.3	12.4	8.3	1.7	3.6	2.5
DY-1-56	1821.6	-24.6	2.08	6.2	74.2	9.3	10.3	1.8	4.1	2.6
DY-1-57	1849.3	-24.9	1.66	16.8	56.8	10.6	15.8	1.8	3.6	2.4
DY-1-58	1876.8	-23.5	1.46	15.2	64.3	8.2	12.3	2.0	3.2	2.6

Abbreviations: Iner. = inertinite; Vit. = vitrinite; Exi. = exinite; Sap. = sapropelinite. Min. = minimum; Max. = maximum; Aver. = average; mmf = mineral matter free.

Table 2

Concentration of the PAHs of ten mudstones from the early Cretaceous Fuxin Basin.

Number	Compound name	Sample number / Concentration of PAHs ($\mu\text{g/g}$ mudstone)									
		DY-1-5	DY-1-8	DY-1-16	DY-1-24	DY-1-26	DY-1-30	DY-1-37	DY-1-40	DY-1-46	DY-1-53
IS	D10-Phenanthrene	0.04141	0.04515	0.02849	0.11199	0.07819	0.07426	0.14018	0.04184	0.15060	0.03929
I	Naphthalene	0.00001	0	0	0	0	0.00399	0	0.00147	0	0
II	Fluorene	0.00061	0.00350	0.01169	0.02711	0.02077	0.03674	0.03862	0.04673	0.03681	0.05182
III	Biphenyl	0.00001	0	0.00294	0.01860	0.00612	0.04734	0.01910	0.09328	0	0.00508
IV	Dibenzothiophene	0.00216	0.00575	0.01254	0.03321	0.03150	0.07033	0.08076	0.11306	0.17462	0.05195
V	Dibenzofuran	0.00037	0.00815	0.09972	0.26086	0.12739	0.29177	0.17239	0.23040	0.00313	0.03044
VI	Phenanthrene	0.05655	0.12072	0.33174	0.88579	0.67586	1.31083	2.03635	2.72338	2.20779	0.75873
VII	Anthracene	0.00110	0.00300	0.00225	0.00275	0.00440	0.00368	0.00166	0.00436	0	0.00913
VIII	Retene	0.00158	0.00423	0.12800	0.21727	0.18751	0.30194	0.08485	0.04924	0.00130	0.01169
IX	Fluoranthene	0.00917	0.05118	0.09612	0.05740	0.03818	0.05019	0.03035	0.03064	0.04148	0.01406
X	Benzo[a]fluorene	0.00021	0.00340	0.00422	0.00493	0.00374	0.00598	0.00618	0.00597	0.00844	0.00160
XI	Benzo[b]fluorene	0.00068	0.01587	0.02661	0.05715	0.04476	0.07620	0.06073	0.05725	0.06277	0.01849
XII	Pyrene	0.00695	0.05776	0.04693	0.07843	0.06009	0.09071	0.13335	0.17908	0.19042	0.06031
XIII	Benz(a)anthracene	0.00027	0.01811	0.01818	0.00485	0.00324	0.00216	0	0	0.00718	0.00259
XIV	Chrysene	0.00044	0.01326	0.01484	0.05154	0.04669	0.10972	0.23315	0.21152	0.24639	0.12779
XV	Benzo[fluoranthenes	0	0.00264	0.00134	0.00363	0	0.00624	0.00853	0.00319	0	0
XVI	Benzo(e)pyrene	0.00040	0.01185	0.00659	0.04256	0.04892	0.08219	0.15981	0.09193	0.06859	0.05603
XVII	Benzo(a)pyrene	0.00037	0.02997	0.00485	0.00733	0.00671	0.00775	0.00714	0.00426	0.00550	0.00197
XVIII	Perylene	0.00053	0.18778	0.04626	0.00069	0.00032	0.00076	0.00179	0	0.00028	0.00049
Total PAHs (more than 3-ring)		0.07825	0.51976	0.72792	1.41431	1.12043	2.04836	2.76389	3.36081	2.84014	1.06287